REVERSE CONVECTION POTENTIAL SATURATION IN THE POLAR IONOSPHERE

Frederick D. Wilder

Thesis submitted to the faculty of the Virginia Polytechnic Institute and State University in partial fulfillment of the requirements for the degree of
Master of Science
in
Electrical Engineering

Dr. C. Robert Clauer, Chair
Dr. Wayne A. Scales
Dr. Scott M. Bailey

April 17, 2008
Blacksburg, VA

Keywords: Ionosphere, Magnetosphere, Electromagnetics, HF Radar, Plasma Physics

ABSTRACT

Reverse Convection Potential Saturation in the Polar Ionosphere

by
Frederick D. Wilder

Chair: Dr. C. R. Clauer

The results of an investigation of the reverse convection potentials in the day side high latitude ionosphere during periods of steady northward interplanetary magnetic field (IMF) are reported. While it has been shown that the polar cap potential in the ionosphere exhibits non-linear saturation behavior when the IMF becomes increasingly southward, it has yet to be shown whether the high latitude reverse convection cells in response to increasingly northward IMF exhibit similar behavior. Solar wind data from the ACE satellite from 1998 to 2005 was used to search for events in the solar wind when the IMF is northward and the interplanetary electric field is stable for more than 40 minutes. Bin-averaged SuperDARN convection data was used with a spherical harmonic fit applied to calculate the average potential pattern for each northward IMF bin. Results show that the reverse convection cells do, in fact, exhibit non-linear saturation behavior. The saturation potential is approximately 20 kV and is achieved when the electric coupling function reaches between 18 and 30 kV/RE.

ACKNOWLEDGEMENTS

I foremost would like to express my most sincere gratitude to my advisor, Professor C. Robert Clauer, who has supported me during the research and also assisted me immensely with his expertise in the field of space science. I'd also like to thank him for all the opportunities to travel and see the world, meeting many exciting people in the process. I would also like to thank Professor Wayne A. Scales for assisting me in my decision to pursue space science as well as introducing me to the field. Thanks also go to Professor Scott M. Bailey for serving on my committee and being a great teacher in aeronomy and atmospheric science.

I would also like to thank Dr. Joseph Baker, for helping to provide me with some of the software to perform this research as well as many helpful discussions on the best way to pursue this phenomenon. I would also like to thank Dr. Valeriy Petrov and Dr. Vladimir (Volodya) Papitashvili for access to the Flat File Software, as well as the MIST virtual global magnetic observatory. Special thanks to Robin Barnes for providing and assisting me with the SuperDARN toolkit.

Finally, I would like to thank my Parents and family who have been very supportive throughout my life and academic career as a whole.

This research is supported by the National Science Foundation through grant ATM-0728538 to the Virginia Polytechnic Institute and State University. Operation of the northern hemisphere SuperDARN radars is supported by the national funding agencies of Canada, France, Japan, the United Kingdom and the United States.

TABLE OF CONTENTS

LIST OF FIGURES

Figure

LIST OF TABLES

Table

LIST OF APPENDICES

Appendix

CHAPTER I

INTRODUCTION

The interactions between the sun and the earth have been a subject of fascination since the dawn of human history. As a blackbody radiator, the sun's irradiance is a crucial driving factor in the regulation of earth's temperature. With the invention of the telescope, scientists such as Galileo Galilei observed the sun's surface and sunspots (*Russell*, 1995). As modern technology and observational capabilities developed, a scientific discipline known as "solar-terrestrial physics" or "space physics" emerged.

Central to solar-terrestrial physics is the interaction between plasma ejected from the sun and the earth's magnetic field. The corona is the outermost layer of the sun's atmosphere. It is an extremely hot gas consisting of ionized hydrogen, free electrons, and helium. Due to a large pressure difference between the corona and interplanetary space, this plasma expands outward into interplanetary space at supersonic speeds and is called the "solar wind" (*Hundhausen*, 1995). Since the sun is constantly rotating, the plasma will also be ejected in a spiral shape, similar to a lawn sprinkler known as the "Parker spiral" (*Hundhausen*, 1995). The Parker spiral is shown in Figure 1.1.

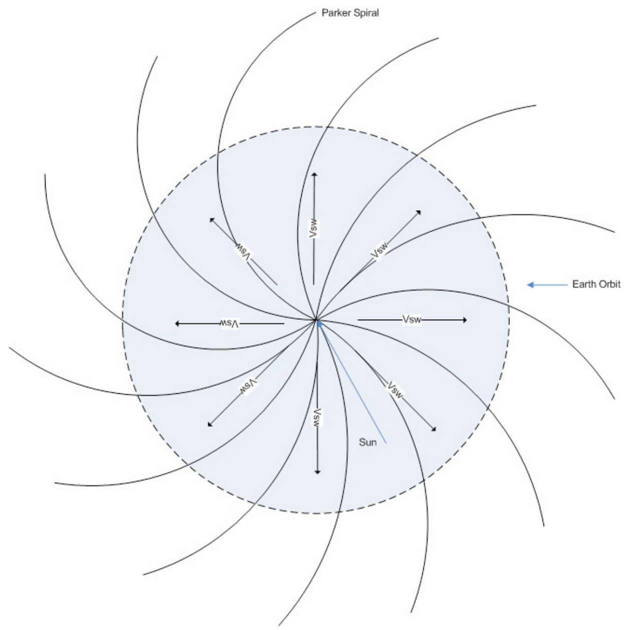

Figure 1.1: Archimedes spiral representation of solar wind propagating at velocity, Vsw (*Hundhausen*, 1995).

1.1 The Interplanetary Magnetic Field

Because of its high conductivity, the solar wind is often assumed to be an ideal Magnetohydrodynamic (MHD) fluid. When describing the time rate of change of the magnetic field, it can be shown that the magnetic induction equation becomes:

$$\frac{\partial \mathbf{B}}{\partial t} = \nabla \times (\mathbf{u} \times \mathbf{B}) \tag{1.1}$$

Where **B** is the magnetic field contained in the solar wind, and **u** is the velocity of the solar wind (*Gurnett and Bhattacharjee*, 2005). Since the (1.1) assumes very large conductivity in the solar wind plasma, there is no term included for the diffusion of the magnetic field. It is thus assumed that the magnetic field is "frozen in" the solar wind and that field lines are carried by the solar wind bulk velocity (*Gurnett and Bhattacharjee*, 2005). This frozen in field is called the "interplanetary magnetic field" (IMF).

For this research, the IMF will be measured in geocentric solar magnetospheric (GSM) coordinates. In this, the origin is at the center of the earth, the z axis contains the projection of the earth's dipole axis, the positive y axis from the origin to local dusk, and the positive x axis points towards the sun, as shown in Figure 1.2(*Kivelson and Russell*, 1995). The Y,Z plane rocks on the x axis as the earth rotates.

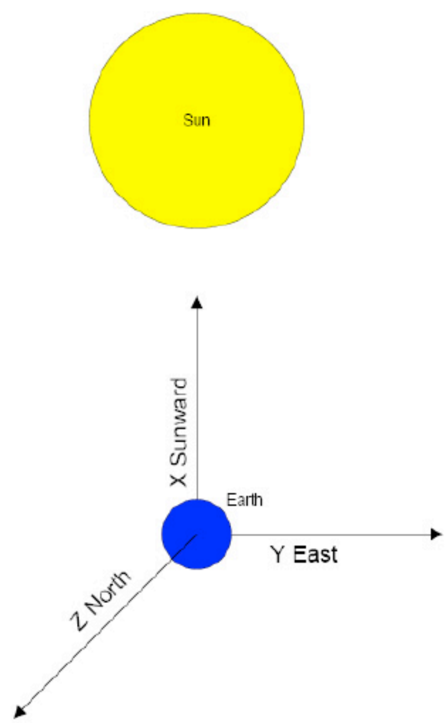

Figure 1.2: The GSM Coordinate System

In MHD, ohm's law is usually given by (1.2).

$$\mathbf{J} = \sigma(\mathbf{E} + \mathbf{u} \times \mathbf{B}) \tag{1.2}$$

Where $\mathbf{J}$ is the electric current density in the plasma, σ is the electrical conductivity of the plasma, and $\mathbf{E}$ is the associated electric field. Due to the frozen in condition, however, the $[\mathbf{E} + \mathbf{u} \times \mathbf{B}]$ term must be negligible to maintain a finite current density (*Hundhausen*, 1995). The associated electric field in the frame of reference of the solar wind plasma is then given by (1.3).

$$\mathbf{E} \approx -(\mathbf{u} \times \mathbf{B}) \tag{1.3}$$

1.2 The Earth's Magnetosphere

As the solar wind flows through interplanetary space, it interacts with planetary magnetic fields in a variety of ways. The Earth's magnetic field, for example, presents an obstacle to the solar wind plasma causing a shock to form upstream. The earth's magnetic field is confined to a cavity in the solar wind flow called the magnetosphere. Due to the dynamic pressure of the solar wind, the magnetosphere is compressed on the day side and drawn into a long comet-like tail behind the earth on the night side (*Walker and Russell*, 1995). The shocked solar wind flows around the magnetosphere in a region called the magnetosheath. The area where the solar wind dynamic pressure is at a standoff with the earth's magnetic pressure is called the "magnetopause" and the subsolar magnetopause distance is typically located at about 10 earth radii (R_E) away from the center of the earth on the dayside (*Walker and Russell*, 1995). Figure 1.3 shows an illustration of a typical interaction between the solar wind and the magnetosphere.

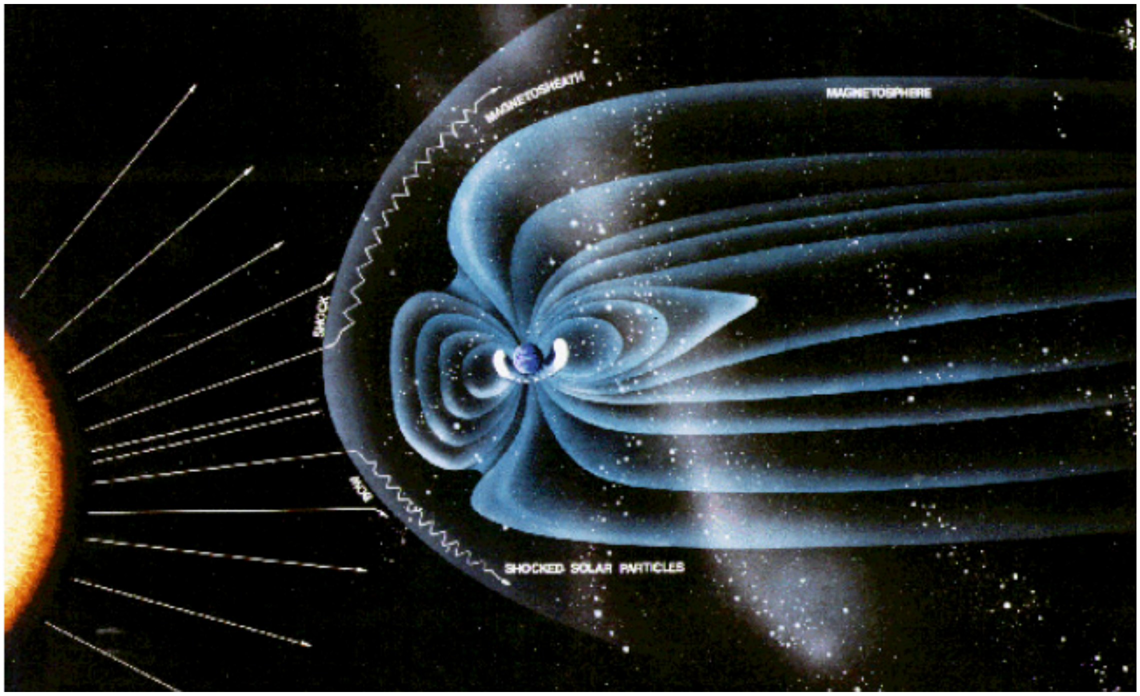

Figure 1.3: An illustration of the solar wind encountering the earth's magnetosphere. Courtesy of NASA Marshal Space Flight Center's Space Plasma Physics Branch. Available at http://science.nasa.gov/ssl/pad/sppb/edu/magnetosphere/images/mag+sun.gif

Large scale convection of plasma within the magnetosphere is tied to various parameters within the solar wind. This convection maps along magnetic field lines into the earth's polar ionosphere, where it can have a direct impact on ionospheric electric fields and thus modern technology. It is therefore important to understand the mechanisms by which magnetospheric convection is driven.

1.2.1 Magnetic Reconnection

The primary mechanism whereby energy and momentum are coupled to the magnetosphere from the solar wind is the process of magnetic reconnection on the day side of the Earth (*Dungey*, 1961). Magnetic reconnection is a process in plasma physics where two anti-parallel magnetic field lines collide at very high pressure, and the field lines literally shear and merge (*Dungey*, 1961). For example, if the IMF is oriented southward when the solar wind encounters the earth's magnetic field, reconnection will occur as in Figure 1.4 (*Dungey*, 1961).

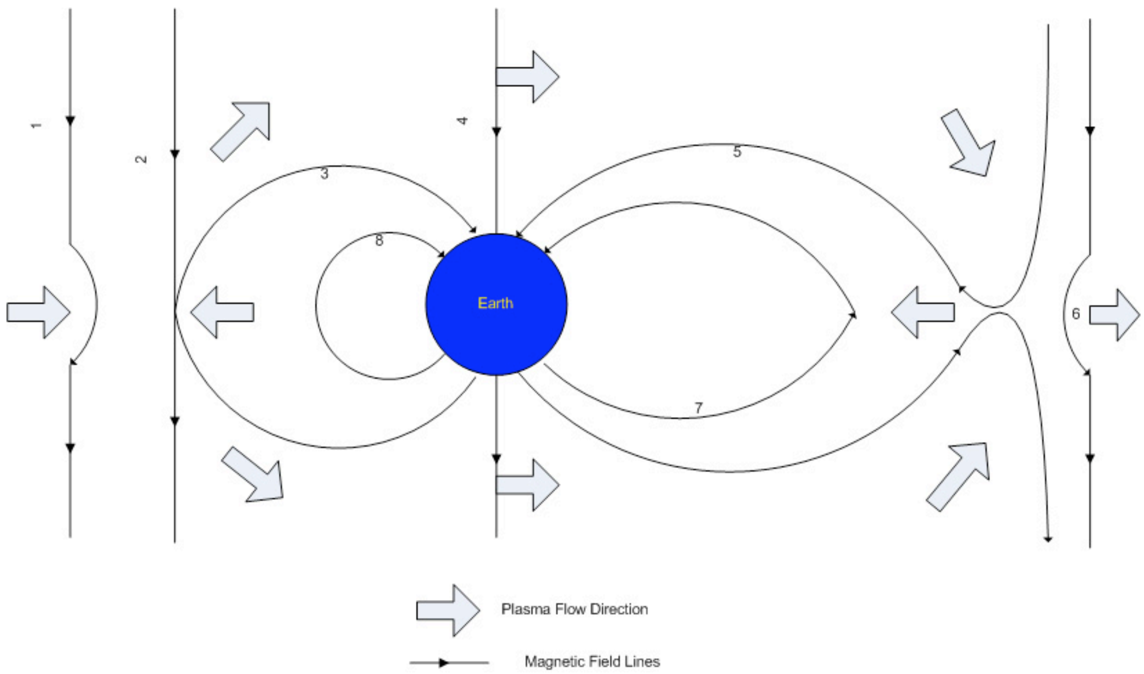

Figure 1.4: Magnetic reconnection and its driving of magnetospheric convection. The IMF (lines 1,2) encounters the earth's magnetic field (line 3) and merges. The two merged field lines split at the reconnection point, forming an x-shaped geometry called the "x-line." The broken field lines are highly bent and thus will feel tension and straighten. This straightening pulls the field lines towards the magnetotail (line 4) and eventually, the lines will reconnect again to close the tail (line 5). The new field line (line 7) attached to the magnetosphere will then flow towards the earth and swing around to the dayside (line 8) where the reconnection process can repeat. The re-formed IMF (line 6) will continue traveling through interplanetary space, adapted from *Dungey* (1961)

Reconnection occurs when the frozen in flux condition breaks down (*Hughes*, 1995). The most common model of reconnection is the Sweet-Parker model, which is illustrated by Figure 1.5.

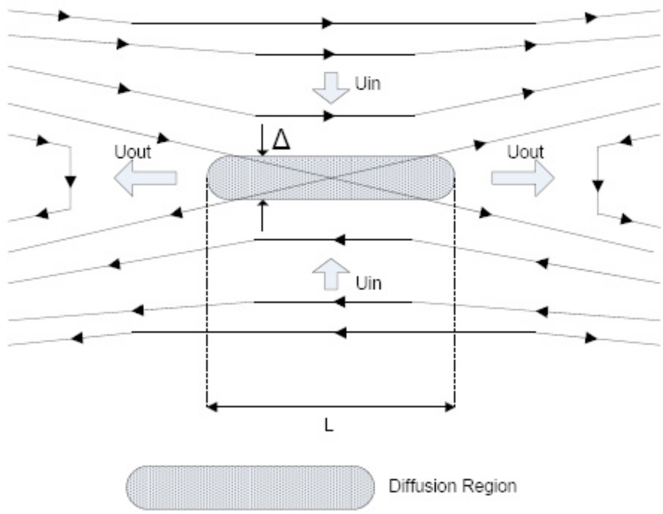

Figure 1.5: The Sweet-Parker model of reconnection (*Gurnett and Bhattacharjee*, 2005).

In the Sweet-Parker model of magnetic reconnection, there is a region in the center of the X-line where the frozen field condition breaks down, called the diffusion region (*Hughes*, 1995). The outflow velocity U_{out} is twice the phase velocity of an MHD wave in the inflowing plasma called the Alfven speed (*Hughes*, 1995).

Magnetic reconnection can also occur when the IMF has other orientations. When the IMF is oriented in an east-west direction, reconnection occurs on the flanks of the earth's magnetosphere, which will skew the resulting magnetospheric convection patterns either in the east or the west (*Friis-Christensen and Wilhjelm*, 1975). When the IMF is oriented northward, the IMF and the magnetic field are anti-parallel at the poleward side of the cusp of the magnetosphere, where the magnetic fields enter and exit the poles (*Dorelli et al.*, 2007). This reconnection orientation is shown by Figure 1.6.

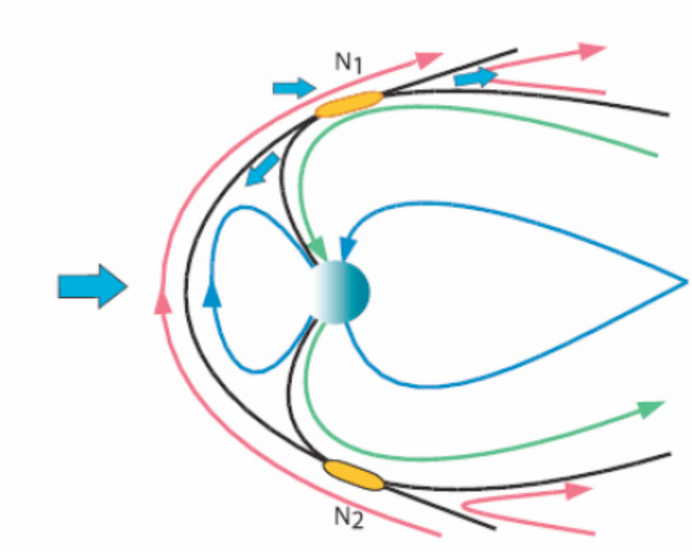

Figure 1.6: Reconnection at high latitudes for Northward IMF. N1 and N2 are the points where the diffusion regions exist, the red field lines are the IMF, and the blue and green lines are the earth's magnetic field. From *Dorelli et al.* (2007)

1.2.2 Viscous Interactions

Another mechanism thought to influence magnetospheric plasma convection is a viscous-like interaction between the solar wind and the earth's magnetic field (*Axford and Hines*, 1961). When a viscous fluid flows over a solid boundary, the viscous effects are confined to a thin layer close to the solid body surface called the "boundary layer" (*Karemcheti*, 1966). Since the velocity at the surface must have a limiting value of zero, but the fluid has non-zero velocity, the boundary layer is an unstable region where the velocity increases rapidly (*Karemcheti*, 1966).

In the magnetosphere, shocked solar wind flows over the surface in a region called the magnetosheath as in Figure 1.3. The magnetosheath plasma has a viscous-like interaction with the magnetosphere, in which a boundary layer is formed (*Sckopke et al.*, 1981). See Figure 1.7 for a representation of the boundary layer at low latitudes. Unlike a fluid flowing over a solid body, the boundary layer of the magnetosphere moves, which causes circulation of plasma throughout the magnetosphere (*Sckopke et al.*, 1981). The higher density region of the boundary layer carries instabilities within it, predominantly what is called the Kelvin-Helmholtz instability (*Kivelson*, 1995). This interaction is analogous to wind blowing over water, driving movement and ripples on the surface.

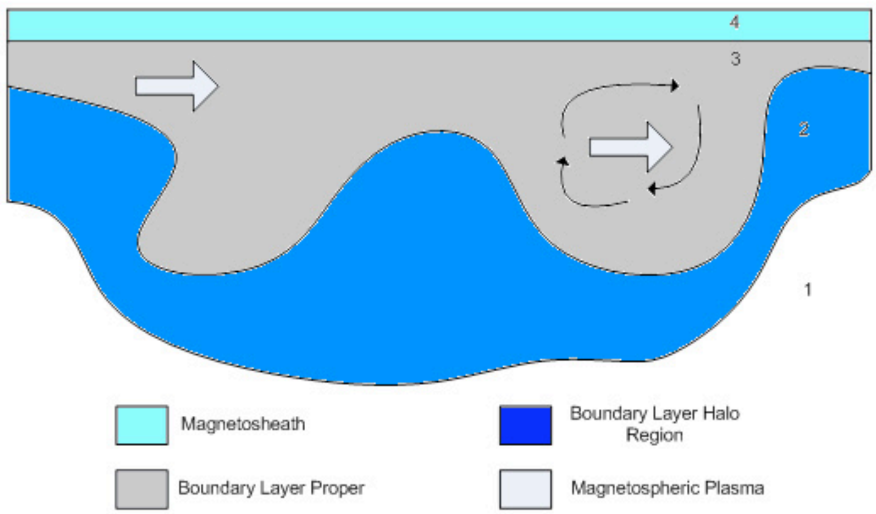

Figure 1.7: The Structure of the Low Latitude Boundary Layer. Region 4 is the solar wind flow, region 3 is the higher density "boundary layer proper" (*Sckopke et al.*, 1981), and region 2 is the halo region where the boundary layer density profile approaches that of the magnetosphere. Kelvin-Helmholtz instabilities determine the shape of region 3 (*Sckopke et al.*, 1981; *Kivelson*, 1995)

.

The viscous drag resulting in the boundary layer drives circulation of plasma throughout the entire magnetosphere (*Axford and Hines*, 1961). The resulting plasma motion is shown in Figure 1.8.

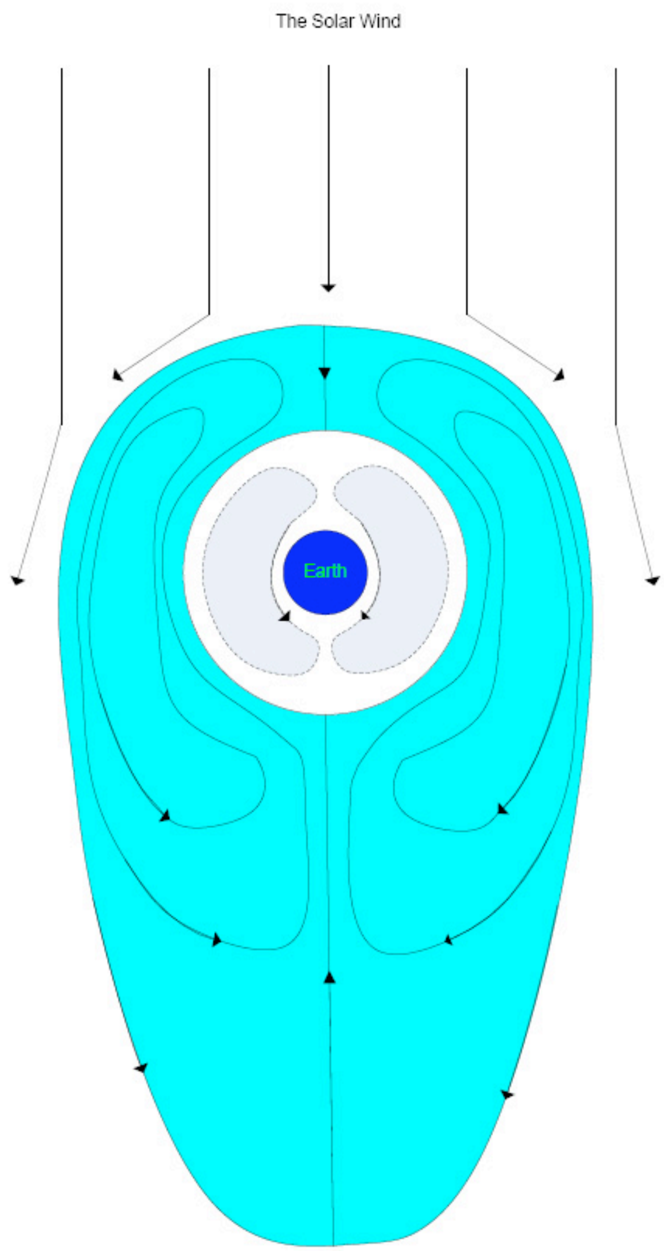

Figure 1.8: Plasma convection in the magnetosphere driven by viscous-like interactions (*Axford and Hines*, 1961)

1.3 Solar Wind - Magnetosphere - Ionosphere Coupling

In the upper regions of earth's atmosphere, solar radiation and particle precipitation can lead to the ionization of various molecules, including O_2, N_2, O and NO

(*Rees*, 1989). Because the ionosphere thus consists of plasma and partially ionized gas, it can have electrodynamic interactions with the earth's magnetosphere. The electric field in the ionosphere can thus be used as a metric of how much energy is transfered in the Solar Wind-Magnetosphere-Ionosphere system.

The earth's magnetic field lines point out of the south pole and point into the north pole. When a large scale effect such as magnetic reconnection with the solar wind occurs, the movement of the magnetic field lines and the resulting plasma convection will be mapped to the high latitude ionosphere (*Dungey*, 1961). This is shown in Figure 1.9, where the high latitude trace lines correspond to magnetic field lines being pulled over the polar cusp, and the low latitude lines correspond to the magnetic field lines being pulled along the center of the magnetosphere back to the earth on the night side (*Dungey*, 1961). A similar convection pattern arises in the absence of reconnection due to viscous-like interactions (*Axford and Hines*, 1961).

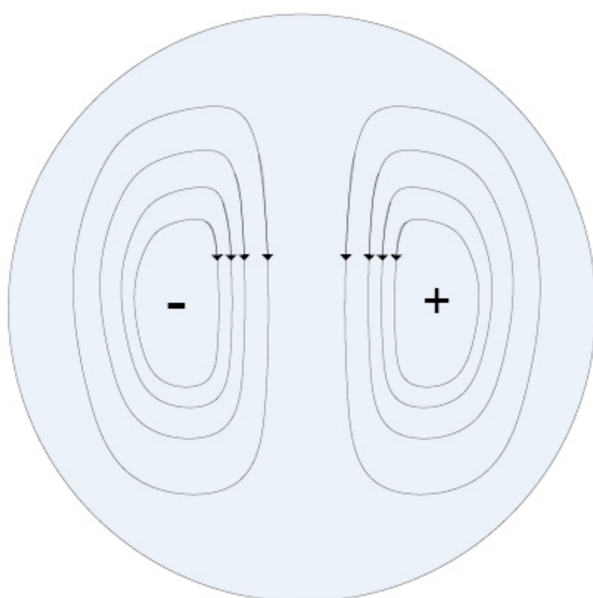

Figure 1.9: The streamlines of ionospheric convection as a result of magnetic reconnection (*Dungey*, 1961). The picture is viewed from above the north magnetic pole looking down. The top of the figure is local noon.

The convection shown in Figure 1.9 is associated with a phenomenon called "Field-aligned Currents" (FACs). Since magnetic fields can be approximated as good conductors (*Chen*, 1974), electric currents move along magnetic field lines into and out of the polar ionosphere called "region 1 currents", leading to a net electric field oriented across the polar cap. When plasma is in the presence of an electric field and a magnetic field, it will have a bulk drift velocity called the $\mathbf{E} \times \mathbf{B}$ drift, given by Equation (1.4) (*Chen*, 1974).

$$\mathbf{v}_{\mathbf{E}\times\mathbf{B}} = \frac{\mathbf{E} \times \mathbf{B}}{B^2} \tag{1.4}$$

Where $\mathbf{v}_{\mathbf{E}\times\mathbf{B}}$ is the drift velocity of the plasma particles and B is the magnitude of the magnetic field. In the northern hemisphere, the magnetic field points into the poles, and so the $\mathbf{E} \times \mathbf{B}$ drift of the Ionospheric plasma at high latitudes will point anti-sunward, or from local noon to local midnight. Applying this analysis to lower latitude field aligned currents that close the system called "region 2 currents", one gets the opposite motion, resulting in the plasma flow vortices shown in Figure 1.10. Applying the same principles, there will be plasma flow vortices in the magnetosphere where the currents close as well. Magnetic reconnection is also thought to generate field aligned currents, as well as compression of plasma (*Friis-Christensen and Wilhjelm*, 1975; *Song and Lysak*, 1995). Field-aligned current systems and current closure in the ionosphere-magnetosphere system will be described in greater detail in Chapter 2.

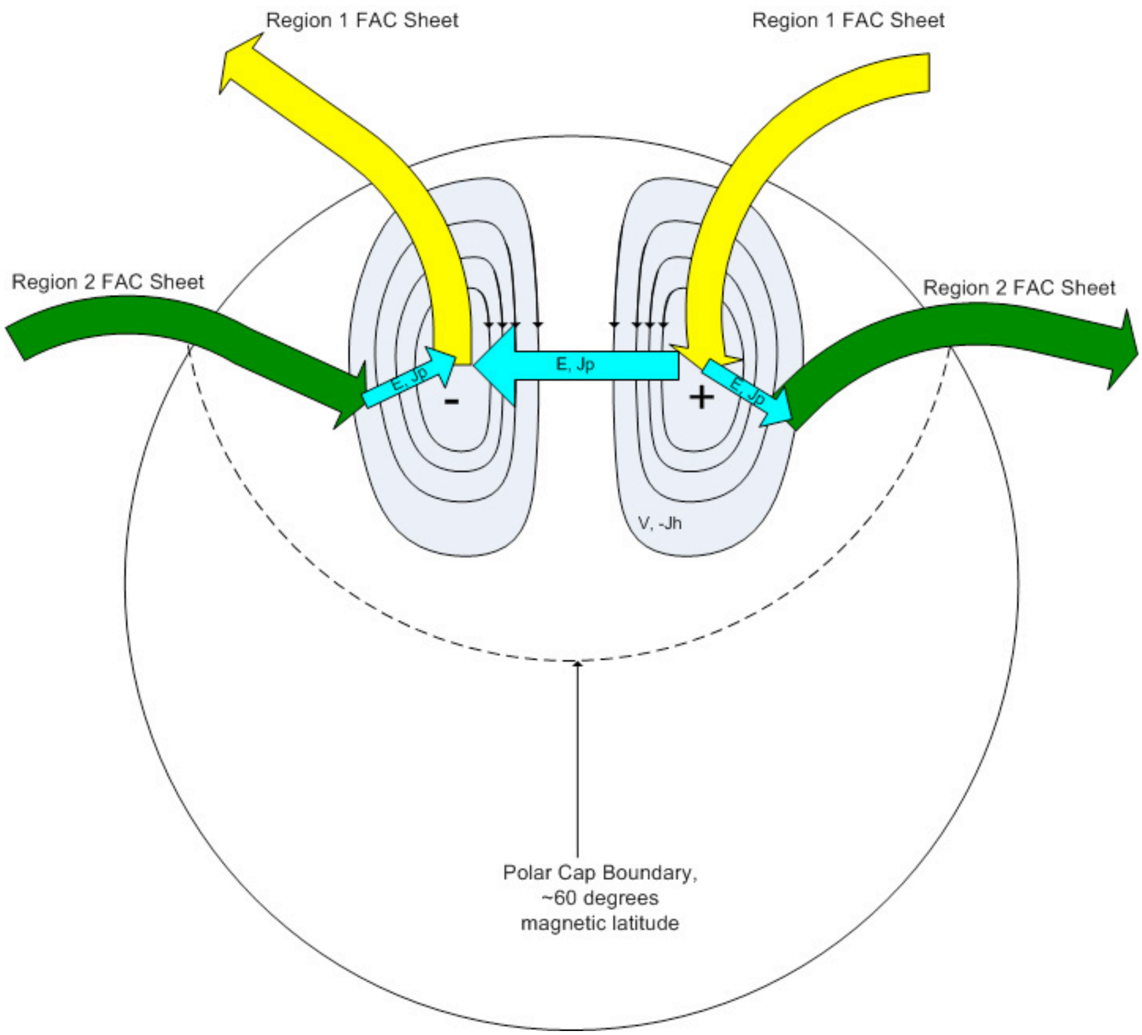

Figure 1.10: An illustration of Region 1 and 2 FACs, as well as the resulting ionospheric electric field (E), plasma convection(V) and electric currents (Jp ad Jh).

Because convecting plasma in a magnetic field has an associated electric field, and because the earth's magnetic field is often assumed to be static, an ionospheric electric potential pattern [$\mathbf{E} = -\nabla\Phi$] is generated. The equipotential lines of the pattern are the streamlines of the plasma convection (*Wolf*, 1995; *Reiff and Luhmann*, 1986). The potential drop across the two convection cells is called the cross polar cap potential, Φ_{PC}, and is an important metric in the Solar Wind-Magnetosphere-Ionosphere system. As the IMF becomes increasingly southward, Φ_{PC} has been observed to exhibit non-linear "saturation" behavior, as shown in Figure 1.11 (*Hill et al.*, 1976; *Siscoe et al.*, 2002b; *Shepherd et al.*, 2002; *Russel et al.*, 2001).

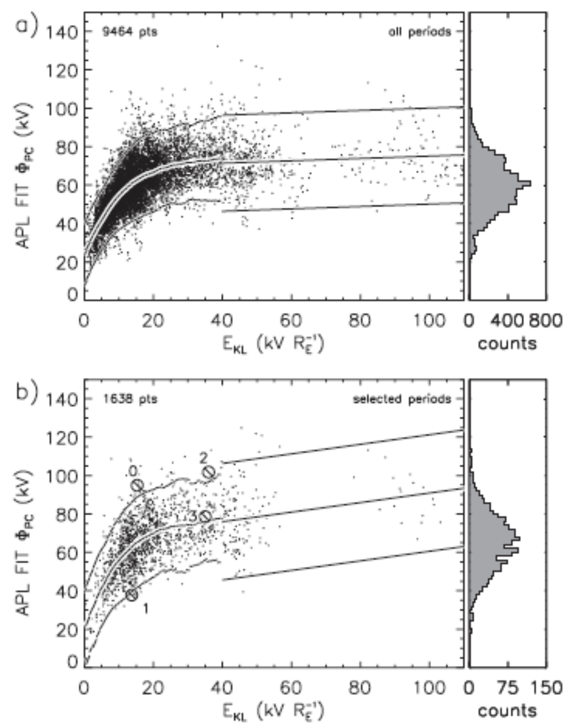

Figure 1.11: A demonstration of Φ_{PC} saturation as a function of E_{KL}, a non-physical coupling metric which represents the electric field of the solar wind before magnetic reconnection. APL FIT is the technique used by the dataset known as the SuperDARN radar to determine the potential across the polar cap (explained in detail in Chapter 3). Count's demonstrates the amount of coverage the SuperDARN radars had for each value of E_{KL}. From *Shepherd et al.* (2002).

For a long time, it was thought that when the IMF was oriented northward, reconnection didn't occur and the magnetosphere system "shut off," making the coupling a half wave rectifier. It was later found that when the IMF is northward, two additional convection vortices appear on the dayside at high latitudes with reversed sunward convection near noon due to magnetic reconnection at the cusp (*Crooker*, 1992). The typical pattern that arises is shown in Figure 1.12. It has yet to be determined if the potential difference across the reverse convection vortices, hereafter referred to as Φ_{RC}, also exhibits non-linear saturation behavior.

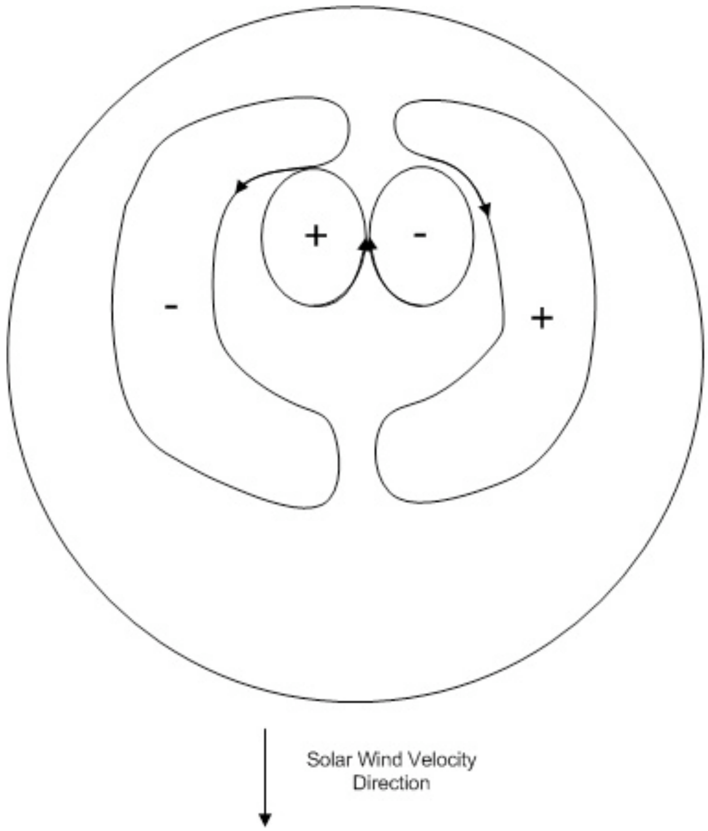

Figure 1.12: An illustration of the convection pattern under northward IMF. The larger cells are the background convection pattern due to viscous-like interactions, and the smaller high latitude cells are due to reconnection near the cusp.

1.4 Motivation

The best possible picture of ionospheric electric field behavior is a crucial aspect of theoretical models and simulations of the Solar Wind-Magnetosphere-Ionosphere system. As field aligned currents close in the ionosphere, the behavior of plasma convection and electrodynamics in the magnetosphere is intricately coupled with the polar ionosphere.

While it has been shown that Φ_{PC} saturates (*Shepherd et al.*, 2002; *Hairston* *et al.*, 2003; *Russel et al.*, 2001), the behavior of Φ_{RC} as a function of increasingly northward IMF has not yet been studied in detail. For the above reasons, it is the purpose of the present study to determine whether the reverse convection cells also exhibits saturation behavior.

CHAPTER II

FIELD ALIGNED CURRENTS UNDER VARIOUS IMF CONFIGURATIONS

2.1 Ionospheric Electrodynamics

2.1.1 Formation of the Ionosphere

The main mechanisms for ionization in the earth's upper atmosphere are photoionization and particle precipitation. With photoionization, high energy UV photons collide with molecules to separate electrons from the nucleus. The three primary photoionization reactions are given by Equations (2.1) through (2.3) (*Rees*, 1989).

$$N_2 + h\nu(< 796\mathring{A}) \longrightarrow N_2^+ + e^- \tag{2.1}$$

$$O_2 + h\nu(< 1026\mathring{A}) \longrightarrow O_2^+ + e^- \tag{2.2}$$

$$O + h\nu(< 911\mathring{A}) \longrightarrow O^+ + e^- \tag{2.3}$$

Where the photon wavelength corresponds to the ionization threshold from the molecule's ground state (*Rees*, 1989). These ions can also collide to form other ions, such as NO^+ (*Carlson and Egeland*, 1995). Another method is the impact of "energetic" electrons, usually with energy greater than 1 keV, precipitating along magnetic field lines from the magnetosphere (*Luhmann*, 1995). Ions can also be lost due to various forms of recombination (*Luhmann*, 1995).

The ionosphere is often categorized in three layers, based on the density of ions and electrons in the gas. These are the D (altitude below 90km), E (altitude between 90 and 130 km) and F (altitude above 130 km) regions (*Luhmann*, 1995). These regions are listed in order of increasing charged particle density.

2.1.2 Ionospheric Conductivity

Due to collisions between ions and neutrals limiting the speed of ions, electric currents can be induced in the ionosphere. It is well known that the ionosphere has anisotropic conductivity, which can be seen in the ionospheric Ohm's law, given by (2.4) (*Richmond and Thayer*, 2000).

$$\mathbf{J} = \sigma_P \mathbf{E}_\perp + \sigma_H \mathbf{b} \times \mathbf{E}_\perp + \sigma_\parallel \mathbf{E}_\parallel \mathbf{b} \tag{2.4}$$

Where $\mathbf{E}$ is the ionospheric electric field, and $\mathbf{b}$ is a unit vector in the direction of the earth's geomagnetic field. The subscripts $\perp$ and $\parallel$ indicate components perpendicular to and parallel to the geomagnetic field, respectively. σ_P, σ_H, and $\sigma_\parallel$ are called the Pederson, Hall and parallel conductivities respectively. As can be seen in Figure 1.10, the Pederson current, $\mathbf{J}_P$, is in the direction of the polar cap electric field and the Hall Current, $\mathbf{J}_H$, is in the opposite direction of the twin cell convection vortices. The expression for the conductivity components are given by Equations (2.5) through (2.7) (*Richmond and Thayer*, 2000).

$$\sigma_\parallel = \frac{N_e e^2}{m_e \left(\nu_{en\parallel} + \nu_{ei\parallel}\right)} \tag{2.5}$$

$$\sigma_P = \frac{N_e e}{B} \left(\frac{\nu_{in}\Omega_i}{\nu_{in}^2 + \Omega_i^2} + \frac{\nu_{en\perp}\Omega_e}{\nu_{en\perp}^2 + \Omega_e^2} \right) \tag{2.6}$$

$$\sigma_H = \frac{N_e e}{B} \left(\frac{\Omega_e^2}{\nu_{en\perp}^2 + \Omega_e^2} - \frac{\Omega_i^2}{\nu_{in}^2 + \Omega_i^2} \right) \tag{2.7}$$

Where N_e is the ionospheric electron density; e is the electron charge; B is the magnetic field magnitude; Ω_j is the frequency a which a charged particle of species

j gyrates around a magnetic field line and is called the cyclotron frequency; ν_{jk} is the collision frequency between particle species j and k; the subscripts $\perp$ and $\|$ correspond to directions perpendicular to and parallel to the geomagnetic field respectively; and the subscripts i, e, and n correspond to the ions, electrons and neutral molecules respectively. A full derivation of Equations (2.5) through (2.7) can be found in *Richmond and Thayer* (2000).

As can be seen from Equations (2.6) and (2.7), if the collision frequency between charged particles and neutrals is much smaller than their cyclotron frequency, the Hall conductivity becomes zero. Therefore, at higher altitudes such as the F-region where the charged particle density is high, the Pederson conductivity will dominate.

Often, Ohm's law is written using a conductivity tensor given by Equations (2.8) and (2.9) (*Gurnett and Bhattacharjee*, 2005).

$$\mathbf{J} = \overleftrightarrow{\sigma}(\mathbf{E} + \mathbf{v} \times \mathbf{B}) \tag{2.8}$$

$$\overleftrightarrow{\sigma} = \begin{bmatrix} \sigma_P & \sigma_H & 0 \\ -\sigma_H & \sigma_P & 0 \\ 0 & 0 & \sigma_{\|} \end{bmatrix} \tag{2.9}$$

Understanding how currents are directed through the ionosphere is crucial to understanding how field-aligned currents close in the coupling between the Solar Wind, Magnetosphere and Ionosphere.

2.2 Field Aligned Currents and Associated Convection Patterns

Although there are debates on small scale generation of field aligned currents, large-scale FACs are thought to be associated with changes in field aligned vorticity in magnetospheric convection cells generated by viscous-like interactions and magnetic reconnection (*Song and Lysak*, 1995). As discussed in Chapter 1.2.1 and 1.3, different orientations of the IMF will generate different convection patterns and therefore different associated field aligned currents.

Friis-Christensen and Wilhjelm (1975) demonstrated that there are different current and convection patterns in the polar cap ionosphere depending on the orientation of the IMF in the Y-Z plane. When the IMF Z component is negative (southward IMF), the two cell pattern shown in Figure 1.9 occurs. When the IMF Z component is zero, and there is a non-zero IMF Y component, then the convection pattern is skewed in either an east or west direction. These skewed patterns are associated with what *Friis-Christensen and Wilhjelm* (1975) termed the "DPY" currents. When the IMF Z component is positive, a four cell convection pattern appears similar to Figure 1.12. The field aligned currents associated with the high latitude reverse convection cells on the dayside in this pattern were termed "NBZ" by *Iijima et al.* (1984).

In the case of reconnection with Southward IMF as well as viscous-like interactions, the electrodynamic coupling between the magnetosphere and ionosphere can be seen in Figure 1.10. At high altitudes, Pederson currents close the current in the ionosphere, related by Ohm's law to the electric field. If the geomagnetic field is assumed to be static, then $\nabla \times \mathbf{E} = 0$ and the electric field can be expressed as the negative gradient of a potential, Φ (*Jackson*, 1975). The drift velocity of the ionospheric plasma can then be expressed by Equation (2.10).

$$\mathbf{v} = -\frac{\nabla\Phi \times \mathbf{B}}{B} \tag{2.10}$$

It can be seen from Equation (2.10) that Φ is a stream-function of $\mathbf{v}$. It follows that equipotential lines given by $\Phi = constant$ represent streamlines of ionospheric plasma flow. A more detailed discussion of streamlines and stream-functions can be found in *Karemcheti* (1966).

When the IMF is oriented northward and the NBZ currents are generated, the current system is more complicated and is shown in Figure 2.1. Region 1 and 2 currents still feed into the ionosphere due to viscous-like interactions, but they are further coupled with the NBZ currents to generate the four cell convection pattern, as well as the potential contours implied by Equation (2.10).

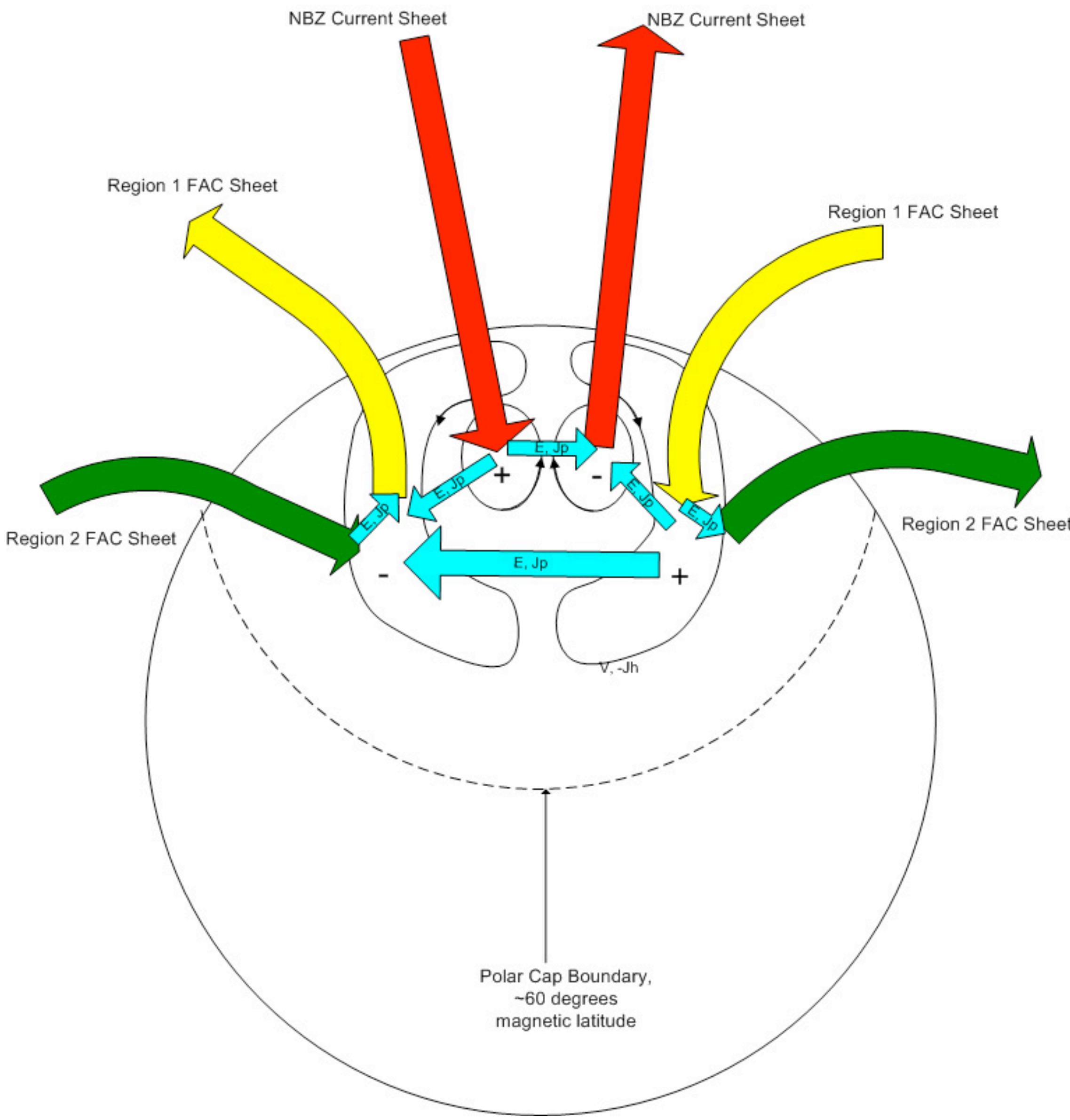

Figure 2.1: An illustration of the field aligned currents and resulting convection during periods of Northward IMF.

In summary, the field-aligned currents associated with various IMF orientations are shown in Figure 2.2, taken from *Weimer* (2001). For northward IMF, the NBZ currents as well as the Region 1 and 2 currents due to viscous-like interactions can be seen, with skewing in the east or west direction when the IMF-Y component is non-zero.

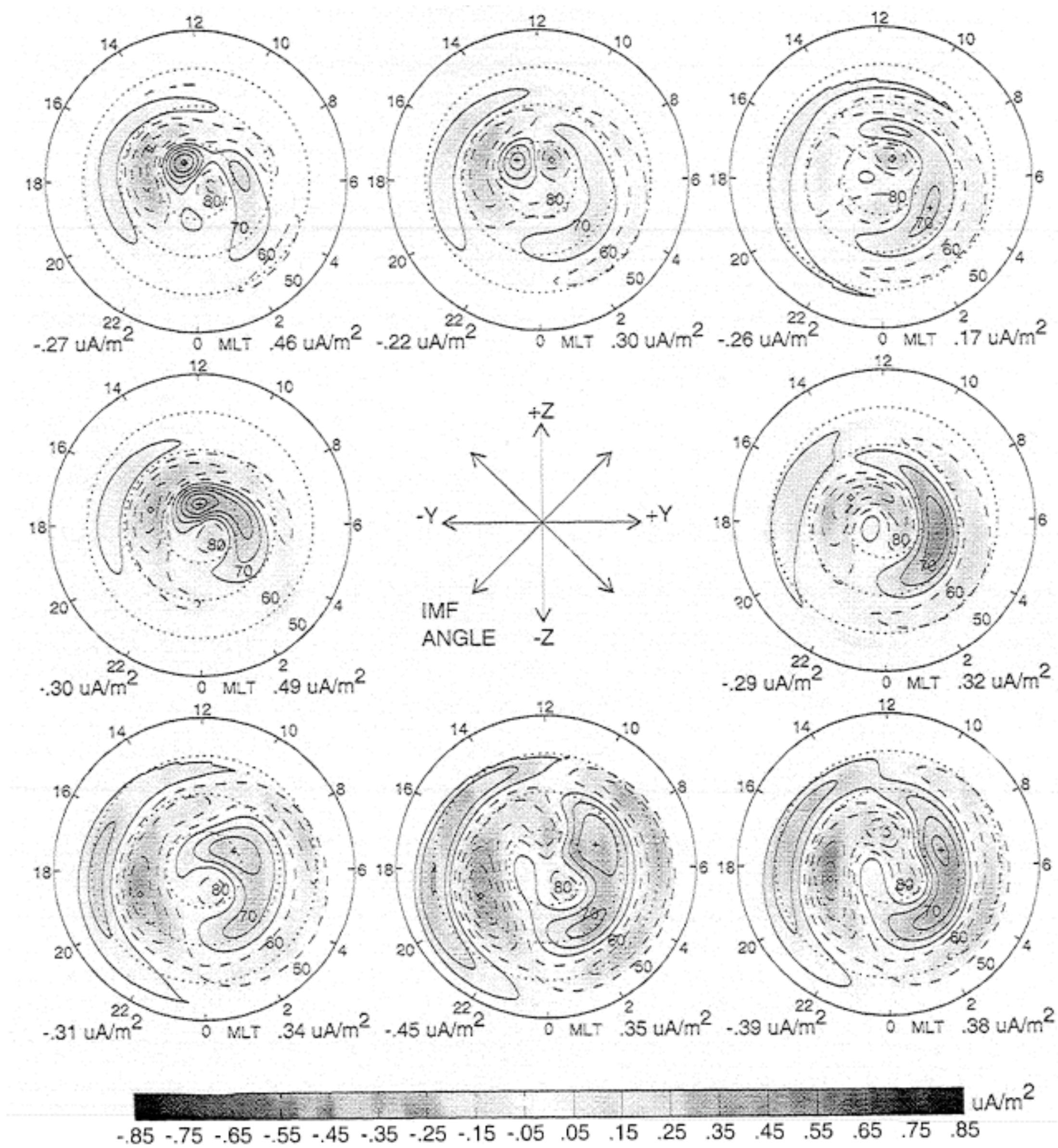

Figure 2.2: Field aligned current maps in the polar ionosphere based on eight different IMF orientations in the Y-Z plane. "The magnitude of the IMF in the GSM Y-Z plane B_T is fixed at 5nT, the solar wind velocity V_{SW} is $400kms^{-1}$, the solar wind proton number density n_{SW}... contours around negative currents are drawn with dashed lines, and solid lines are used for positive currents, with the convention that positive currents are into the ionosphere. The magnitude of the current is also indicated with the intensity of the grey scale shading"(*Weimer*, 2001).

2.3 Transpolar Potential Saturation and Existing Models

The electric potential existing across the two cells shown in Figure 1.9 is usually called the "Cross Polar Cap Potential," and shall be denoted Φ_{PC}. It was originally thought that as the IMF turned increasingly southward, Φ_{PC} would increase linearly with the interplanetary electric field (IEF). The idea was that a fraction of the solar wind electric field would be impressed upon the magnetosphere, generating a magnetospheric convection potential, Φ_m. This large scale potential would then map along magnetic field lines into the polar ionosphere, with Φ_{PC} being approximately equal to Φ_m (*Hill et al.*, 1976; *Reiff and Luhmann*, 1986; *Siscoe et al.*, 2002b).

An alternative to the linear model was that by some undefined mechanism, Φ_{PC} would eventually become non-linear, and reach a saturation value similar to that seen in Figure 1.11 (*Hill et al.*, 1976; *Siscoe et al.*, 2002b). This saturation model was called the Hill Model of Saturation, and is given by Equation (2.11) (*Siscoe et al.*, 2002b).

$$\Phi_{PC} = \frac{\Phi_m \Phi_S}{\Phi_m + \Phi_S} \tag{2.11}$$

Where Φ_S is called the "Saturation Potential." In the Hill Model, when $\Phi_m << \Phi_S$, then the polar cap potential is approximately equal to the magnetospheric potential. When $\Phi_m >> \Phi_S$, the polar cap potential will be approximately equal to the saturation potential. Empirical studies have demonstrated the Saturation Model to be more accurate than the linear model, with Φ_S found to be between 100 and 200 kV (*Siscoe et al.*, 2002b; *Shepherd et al.*, 2002; *Russel et al.*, 2001).

Several models have been proposed based on MHD simulations that attempt to explain the saturation phenomenon. One model suggests that Region 1 FACs weaken the earth's magnetic field in at the magnetopause, limiting reconnection. A similar model states that a dimple in the magnetic field forms at the stagnation point in solar wind flow, which also limits reconnection (*Siscoe et al.*, 2004). Another model, given by (*Siscoe et al.*, 2002a), is that Region 1 FACs saturate when they become strong enough that their $\mathbf{J} \times \mathbf{B}$ force can balance out the dynamic pressure of the solar wind. A fourth model involves the magnetopause becoming blunt, which widens the magnetosheath. The solar wind then has more room in the magnetosheath to flow past the magnetosphere, limiting reconnection (*Siscoe et al.*, 2004). *Nagatsuma* (2004) also observed that the saturation phenomenon is partially determined by the conductivity of the ionosphere. As the solar zenith angle decreases and the Pederson conductivity of the ionosphere increases, the saturation phenomenon becomes more pronounced (*Nagatsuma*, 2004).

While it has been demonstrated that convection cells associated Region 1 and 2 FACs saturate, there have been no observations of the trend in the reverse convection cells associated with the NBZ Currents. Comparing the geometry of reconnection in the case of southward and northward IMF (Figures 1.4 and 1.6 respectively), one can see the impact on the current models for Φ_{PC} saturation. Since during northward IMF, reconnection occurs at the high latitude edge of the cusp, a strengthening of the NBZ currents could not have the same effect that the Region 1 currents have at the equatorial magnetopause. Therefore, it is crucial to determine whether the NBZ currents saturate.

CHAPTER III

METHODOLOGY

In order to determine if the reverse convection potential associated with the NBZ current system saturates, several steps were taken. First, a large amount of events where the IMF is steadily northward were found. These events were then sorted and binned based on the strength of the solar wind electric field. Ionospheric convection data from the Super Dual Auroral Radar Network (SuperDARN) (*Chisham et al.*, 2007) was then be compiled to generate convection patterns for each bin to get a convection map, from which the potential pattern was inferred. Once a convection potential is obtained, the potential across the high latitude dayside reverse convection cells, Φ_{RC} can be measured for each bin.

3.1 Solar Wind Data Analysis

3.1.1 The ACE Satellite

All solar wind and IMF data was taken from the Advanced Composition Explorer (ACE) satellite. This satellite orbits around the L1 point, which is one of the Lagrange points where the gravitational fields of the earth and the sun cancel. The L1 point is upstream in the solar wind between the earth and the sun between the earth's day side and the sun. For this reason, it is a prime location to measure solar wind parameters before they reach the earth. There are two instruments on ACE. MAG measures the components of the magnetic field vector and SWEPAM measures plasma parameters such as composition, density, velocity and temperature (*Stone et al.*, 1998).

A complication in using ACE satellite data is the delay between a measurement the satellite makes and the time it takes for that measurement to reach the earth's magnetopause. As can be seen from Figure 3.1, depending on where the ACE satellite is in its orbit around the L1 point, it will see a different point on the Parker Spiral. Thus, the earth's magnetopause might see the measurement earlier or later than the expected time of travel between the L1 point and the magnetopause (*Ridley*, 2000). There are several methods to calculate when a measured parameter will hit the magnetopause, but the data used in this study was pre-propagated UCLA data which used the minimum variance technique outlined by *Weimer et al.* (2003). The error of propagation time estimates can be on the order of a few minutes, and thus will effect time selection criteria when the effects of Northward IMF are measured (*Ridley*, 2000).

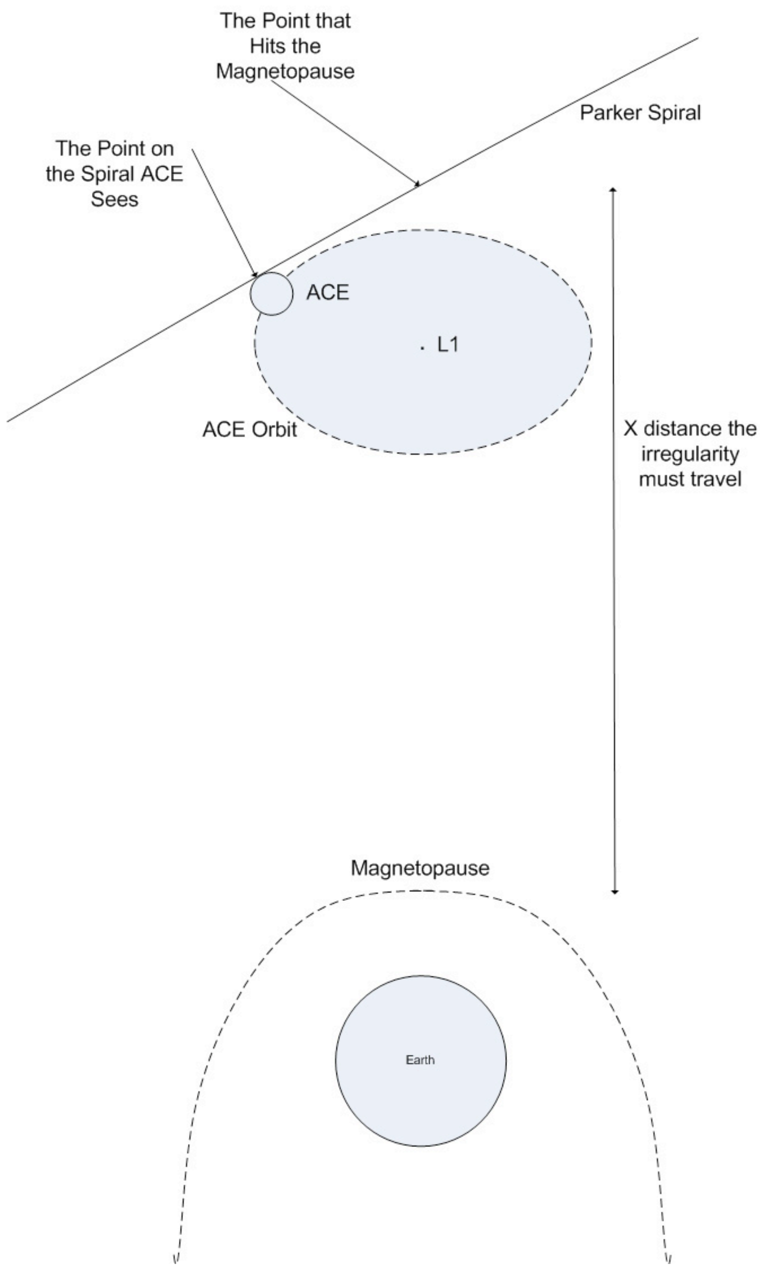

Figure 3.1: A picture of the ACE orbit with respect to the magnetopause and the parker spiral.

3.1.2 The Energy Coupling Function

In order to determine the response of the reverse convection potential to the solar wind, there must be a metric which represents how much of the interplanetary electric field (IEF) is coupled into the ionosphere from the solar wind. *Kan and Lee*

(1979) developed a metric which was used by *Shepherd et al.* (2002) in their study of the polar cap potential saturation response to southward IMF conditions, called the "energy coupling function." The energy coupling function for southward IMF is given in equation (3.1).

$$E_{kl} = V_x B_T sin^2 \frac{\theta}{2} \tag{3.1}$$

Where V_x is the x component of the solar wind velocity, $B_T = \sqrt{B_y^2 + B_z^2}$ is the component of the IMF transverse to the solar wind bulk velocity, and $\theta = cos^{-1} \frac{B_z}{B_T}$ is called the IMF clock angle, which represents the orientation of the IMF in the Y-Z (GSM) plane. Equation 3.1 is loosely based on the frozen field theory given by Equation 1.3 and is measured in kilovolts per earth radii (kV/R_E). The equation is derived assuming that the solar wind bulk velocity only travels in the x direction, which is reasonable (*Kan and Lee*, 1979).

When the IMF is purely northward, there will be a clock angle of zero degrees, and the sine term in equation (3.1) will be zero. Thus, in order to study the behavior of reverse convection cells, another metric must be used. Since the sine term is a non-physical geometric scaling factor, it can be altered to look for events where high latitude reverse convection cells would form. If one assumes that a pure y IMF would not generate reverse convection and that the y-component of the IMF only affects the skew of the reverse cells, the energy coupling function can be modified as shown in Equation (3.2).

$$E_{RC} = -V_x B_T cos^n \theta \tag{3.2}$$

This will always be positive as long as the value of n is an even integer and the clock angle is between -90^o and 90^o. The value of the exponent will directly effect how much the y component of the IMF impacts the value of E_{RC}. The larger n is, the more the y component will reduce the coupling function's magnitude. Plots of these functions for $n = 2$ and $n = 4$ can be seen in Figures 3.2 and 3.3.

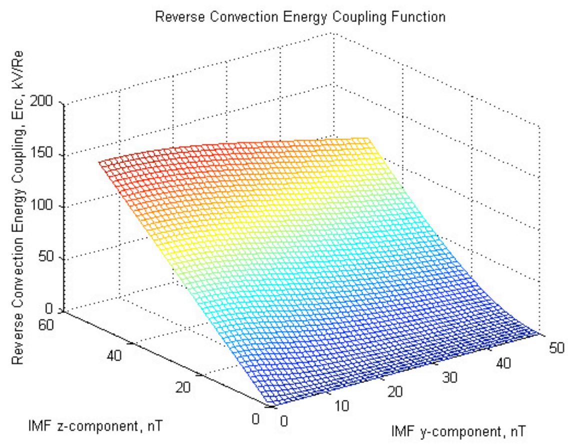

Figure 3.2: E_{RC} versus the IMF y and z component for solar wind with a bulk velocity of 500 km/s and $n = 2$

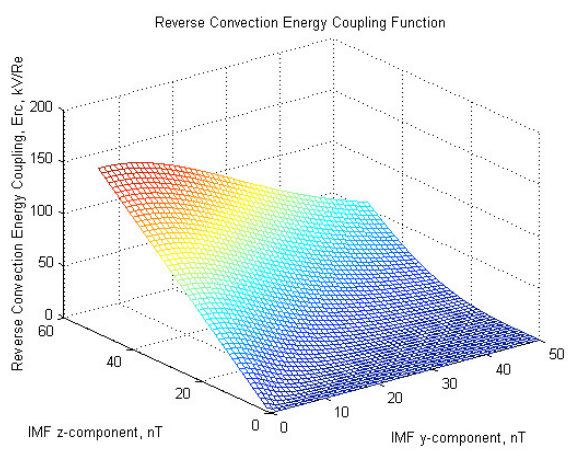

Figure 3.3: E_{RC} versus the IMF y and z component for solar wind with a bulk velocity of 500 km/s and $n = 4$

In this study, $n = 4$ will be used. As seen in Figure 3.3, an exponent of four limits the influence of the IMF-y component. Also, $n > 4$ was not used because Super-

DARN would not have enough doppler measurements to produce enough accurate maps to cover the range of Figure 4.2.

3.2 Ionospheric Electric Potential Mapping

3.2.1 The Super Dual Auroral Radar Network

The Super Dual Auroral Radar Network (SuperDARN) is a network of high latitude coherent scatter radars which work in conjunction to produce large scale convection patterns in the polar ionosphere. As of 2007 there were 11 radars in the northern hemisphere and 7 radars in the southern hemisphere, with a diagram of the locations and overlap given in Figure 3.4. A detailed list of all radars and their geographic and geomagnetic location Additional radars have been constructed since 2007, but their doppler measurements have not been used in the present study.

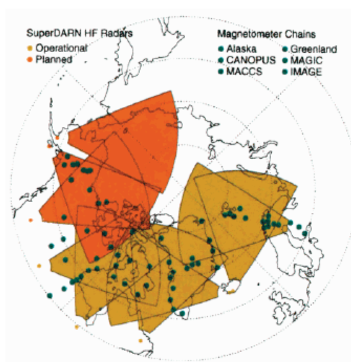

Figure 3.4: Coverage of the SuperDARN radars in the northern hemisphere. From *Ruohoniemi and Baker* (1998).

A SuperDARN radar operates at the high frequency (HF) band of the radio spectrum, and is typically capable of transmitting at center frequencies between 8 and 20 MHz (*Chisham et al.*, 2007). The major mechanism by which the radar calculates line of sight plasma drift velocities is by backscatter from ionization density irregularities aligned with the geomagnetic field. At 10.8 MHz, the signal is sensitive to irregularities with a wavelength of 13.9 m and studies have shown that in the F region the irregularities which produce backscatter convect with the $\mathbf{E} \times \mathbf{B}$ drift of the plasma (*Ruohoniemi et al.*, 1987). They have also been demonstrated to be a common occurrence in the high-latitude regions of the ionosphere (*Ruohoniemi et al.*, 1987). The signal incident on the irregularities must be approximately orthogonal to the geomagnetic field lines, and thus the scatter is actually assisted by the refraction of the signal in the ionosphere (*Ruohoniemi et al.*, 1987; *Ruohoniemi and Greenwald*, 1996; *Chisham et al.*, 2007).

In order to obtain the large scale convection pattern, several steps must be taken. First, the line of sight velocities calculated by the each radar are placed into spatial bins with a width of 1 degree of latitude and 10 degree increments of magnetic azimuth, and the values are averaged within each bin (*Ruohoniemi and Baker*, 1998). An example of these bins and the resulting average line of site velocities for a specific event are given by Figures 3.5 and 3.6.

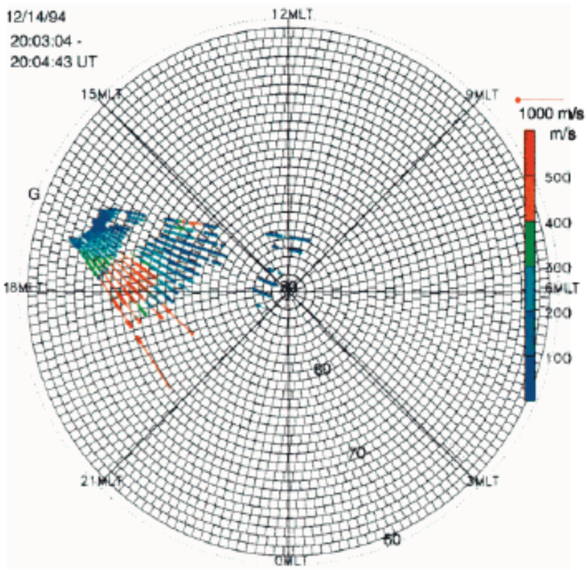

Figure 3.5: An example of the grid used for averaging the line of sight velocity vectors. The velocity data is taken from the Goose Bay Radar on December 14, 1994, from 2003-2004:43 UT. From *Ruohoniemi and Baker* (1998).

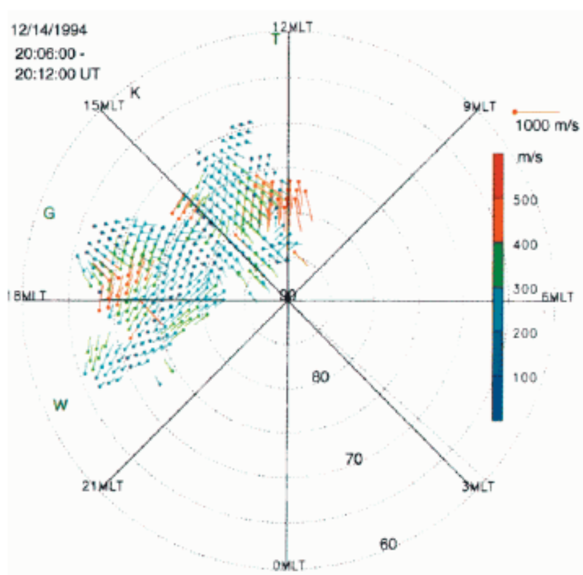

Figure 3.6: Averaged line of site velocities from SuperDARN radars in Saskatoon, Kupaskasing, Goose Bay and Stokkseyri on December 14, 1994, 2006-2012 UT. Taken from *Ruohoniemi and Baker* (1998)

Once the spatially averaged line of site velocities are calculated, line of site velocities in areas where the fields of view of two or more radars can be resolved into convection velocity vectors. If more than two radars overlap, a least square error fit is used (*Ruohoniemi and Baker*, 1998). Figure 3.7 shows the result when the LOS velocity vectors given in Figure 3.6 are resolved. Areas with no overlap are not included (*Ruohoniemi and Baker*, 1998).

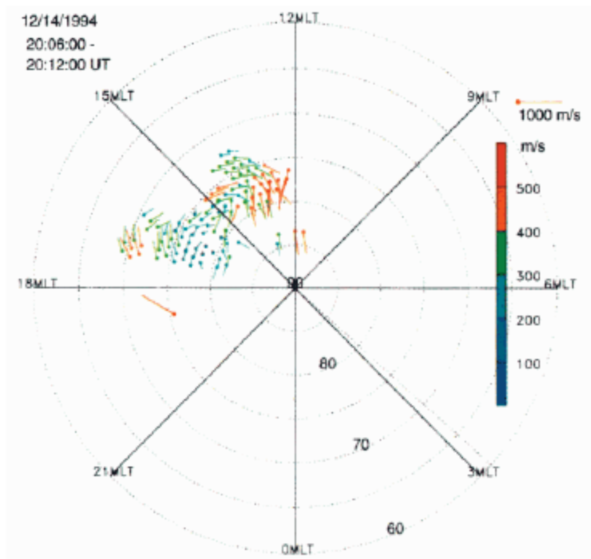

Figure 3.7: The velocity vectors resolved from the LOS vectors in Figure 3.6. From *Ruohoniemi and Baker* (1998)

3.2.2 Spherical Harmonic Mapping of the Ionospheric Electric Potential

Once ionospheric velocity vectors have been calculated by SuperDARN, one can proceed to calculate the ionospheric potential pattern, Φ. This is done by assuming that the geomagnetic field is stationary and that the net charge density in the ionosphere is zero. In this case, the ionospheric electric potential can be found using Laplace's Equation (3.3) (*Jackson*, 1975).

$$\nabla^2 \Phi = 0 \tag{3.3}$$

If the potential is assumed to exist on the surface of a spherical earth, then the solution of Laplace's equation is a spherical harmonic expansion given by Equation (3.4) (*Weimer*, 1995; *Jackson*, 1975).

$$\Phi(\theta, \phi) = \sum_{l=0}^{\infty} \sum_{m=-l}^{+l} A_{lm} \sqrt{\frac{2l+1}{4\pi} \frac{(l-m)!}{(l+m)!}} P_l^m(\cos\theta) e^{im\phi} \tag{3.4}$$

Where θ is the co-latitude and ϕ is the azimuthal angle on the surface of an arbitrary sphere, and P_l^m is the Legendre polynomial. For the ionospheric potential, θ and Φ can be explained in terms of geomagnetic coordinates by Equations (3.5) and (3.6) (*Weimer*, 1995).

$$\theta = (90 - MLAT)\frac{pi}{45} \tag{3.5}$$

$$\phi = MLT\frac{pi}{12} \tag{3.6}$$

Where MLAT is the magnetic latitude and MLT is the magnetic local time. MLAT is the latitude based on the location of the magnetic north pole, not the geographic one. MLT is the location where it is at a certain time. For example, MLT noon would be the magnetic longitude line which directly faces the sun and MLT midnight would be the magnetic longitude line facing opposite the sun.

Since it was shown by Equation (2.10) that the plasma convection velocity in the ionosphere flows on equipotential lines, an electric potential pattern can be fit to convection data (*Weimer*, 1995; *Ruohoniemi and Baker*, 1998).

SuperDARN uses a routine called APLFIT to fit velocity vectors to a spherical harmonic expansion. Coefficients are calculated to minimize the χ^2 value for the LOS component of the velocity vectors (*Ruohoniemi and Baker*, 1998). Because χ^2 is defined for the LOS component, even vectors where there is no overlap may be used in the spherical harmonic fit. Also, to fill in spaces with no coverage, statistical patterns based on IMF orientation are used (*Ruohoniemi and Greenwald*, 1996). The result of APLFIT applied to the velocity LOS vectors given in Figure 3.6 is shown in Figure 3.8.

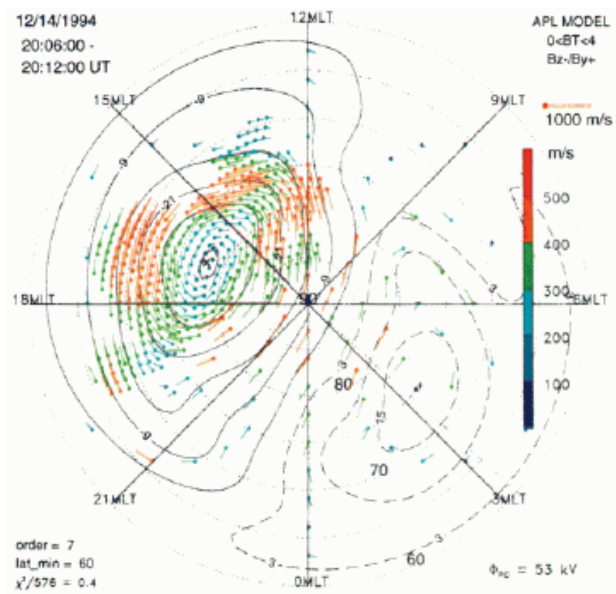

Figure 3.8: The convection and potential pattern fit to the LOS vectors in Figure 3.6. The order of the expansion is 7. From *Ruohoniemi and Baker* (1998)

3.3 Event Selection Criteria and Convection Map Averaging

3.3.1 Solar Wind and IMF Stability Criteria

Using E_{RC}, events were found using ACE MAG and SWEPAM data from 1998 to 2005. Events of quasi-stable E_{RC} were then placed into bins containing a minimum and maximum E_{RC} value. The criteria for quasi-stability was that the event stayed within the bin's maximum and minimum E_{RC} value for a minimum of 40 minutes. The minimum event duration was chosen to account for solar wind propagation estimation delays, as well as the time it takes for the reverse convection cells to form after a northward turning of the IMF (*Clauer and Friis-Christensen*, 1988). The E_{RC} range for each bin was selected to maximise the spatial coverage of Doppler measurements by SuperDARN in each bin, but at the same time provide enough discretization for the curve in Figure 4.2 to see the saturation effect. Table 3.1 shows the range of each bin, as well as the number of quasi-stable events.

Table 3.1: Bins of E_{RC} Used To Generate Figure 4.2

Range (kV/R_E)	Events	Range (kV/R_E)	Events	Range (kV/R_E)	Events
0-2	4,286	19-23	33	31-38	10
2-4	175	20-24	38	31-40	25
4-6	79	21-25	31	32-36	11
10-16	65	22-26	26	32-39	15
12-15	54	23-27	20	37-47	13
13-16	45	24-28	15	40-50	15
14-18	27	25-30	23	43-53	10
16-19	22	27-32	21	46-56	8
16-21	26	28-36	26		
18-22	33	30-36	11		

3.3.2 Convection Map Averaging

For a given bin of E_{RC}, velocity vectors from 20 minutes into each quasi-stable event were further divided into spatial bins on a grid of 100km and 10-degree increments of magnetic azimuth. The median value in each spatial bin was then calculated. This pre-processing reduces the amount of data which goes into the spherical harmonic fitter. It is also beneficial because it smoothes out large positive and negative values which cancel in the fitter at convection reversal boundaries. The APLFIT technique was then applied, deriving the electric potential pattern. Velocity vectors from the SuperDARN statistical model were not used to generate the potential patterns so as not to bias the results. Figure 4.1 shows the results of the spherical harmonic fit for several bins of E_{RC}. Once an E_{RC} bin's potential pattern is calculated, Φ_{RC} can be found by measuring the potential between the reverse convection cells, circled in red in Figure 4.1.

CHAPTER IV

RESULTS AND DISCUSSION

Figure 4.1 shows four convection patterns as the IMF turns increasingly northward. Each pattern is presented in AACGM MLAT-MLT format with the magnetic pole at the center and magnetic noon directed up the page. The lowest latitude shown is 60 degrees and the contour spacing is 1kV. Color-coding shows the number of gridded SuperDARN measurements that contributed to the calculation of each pattern. The four convection patterns in Figure 4.1 correspond to the following bins of E_{RC}: (a) 2-4, (b) 10-13, (c) 19-23, and (d) 32-39 kV/RE. The values of the reversed convection potential, Φ_{RC}, are 2.85, 10.66, 17.44, and 19.36 kV respectively. The reader is invited to count the potential contours across the dayside reverse convection cells to demonstrate these potential values. Appendix A contains average convection maps for all of the E_{RC} bins used in the present study.

4.1 Results and Discussion

As seen in Figure 4.1, as the value of E_{RC} increases, the reversed convection cells first become more pronounced but then the reversed convection potential eventually saturates. Also note that as the value of E_{RC} is allowed to increase the number of SuperDARN measurements available to calculate the pattern also decreases. Beyond

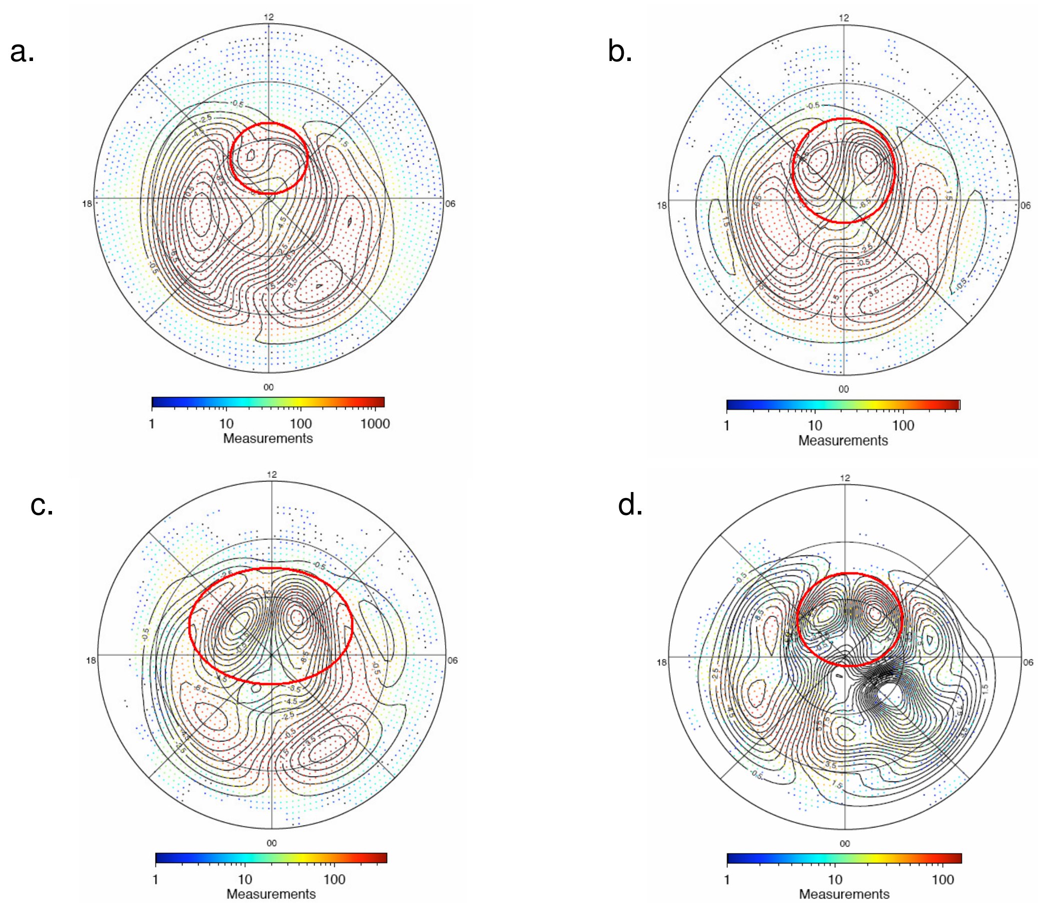

Figure 4.1: Calculated four cell convection pattern for four E_{RC} bins: a) 2 to 4 kV/Re, b) 10 to 13 kV/Re, c) 19 to 23 kV/Re and d) 32 to 39 kV/Re. The dayside convection cells are circled in red.

60 kV/RE there were too few Doppler measurements available to calculate a potential pattern.

Figure 4.2 shows a plot of the reverse convection potential for E_{RC} values up to 70 kV/RE. The horizontal bars show the range of values used in each E_{RC} bin used to calculate each convection pattern. For low values of E_{RC} (i.e. 0-18 kV/RE) the reverse convection potential exhibits linear characteristics but as E_{RC} increases the reverse potential starts to saturate, similar to what has been identified previously for southward IMF (*Shepherd et al.*, 2002). The rapid decrease in the slope of Φ_{RC} can clearly be seen in the E_{RC} range 20 to 26 kv/RE.

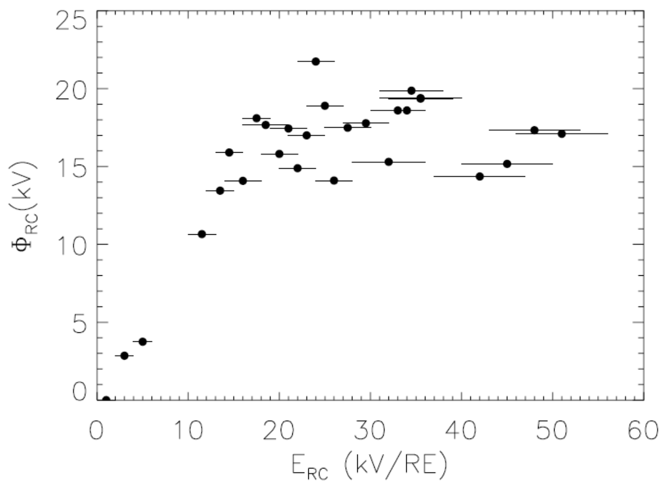

Figure 4.2: The reverse convection potential, Φ_{RC}, as a function of E_{RC}. The marks represent the center of the bins, and the horizontal lines represent the width of each bin in kV/Re

It is still unclear at this time why the NBZ currents and the potential across the vortices they generate should saturate. In the case of southward IMF, there are several models that account for saturation of Φ_{PC}. Three common models are: the strengthening of Region 1 field aligned currents to the point where their $\mathbf{J} \times \mathbf{B}$ force replaces the currents at the magnetopause as the main counter to solar wind ram pressure; the erosion of the magnetopause magnetic field which limits reconnection; and the magnetopause becoming blunt, giving the solar wind more room to flow around the magnetosphere (*Siscoe et al.*, 2004). All of these models are related to the strength of the Region 1 field-aligned currents. Since the NBZ currents are driven by reconnection at the cusp, it is unlikely that these models could also be applied to saturation of the reverse convection cells. One thing that hasn't been investigated is whether or not there is a limit to the amount of current the ionosphere can carry. If it is the case that the ionospheric conductivity plays a role, then it could help explain the saturation phenomenon for both the southward and northward IMF cases.

For further study, case studies of events with even stronger E_{RC} will be done combining high latitude radar and satellite data. Analysis of the reverse convection cell response time will also be done, as well as further analysis of the transition from linear to non-linear behavior. The Canadian high latitude PolarDARN radars, as well as the Resolute Bay incoherent scatter radar when it begins operation, will also give more coverage to the regions where reverse cells form, and at the next solar maximum, a better picture of the reverse convection potential during strong IMF will be developed. This will assist in determining as well as possible the maximum potential the reverse convection phenomena can generate. Also, comparing electric fields with the Southward IMF case and looking for seasonal asymmetries would help to determine how much current can pass through the ionosphere at a given time, as well as the effects of conductivity.

APPENDICES

APPENDIX A

SuperDARN Plots Used to Generate Saturation Curve

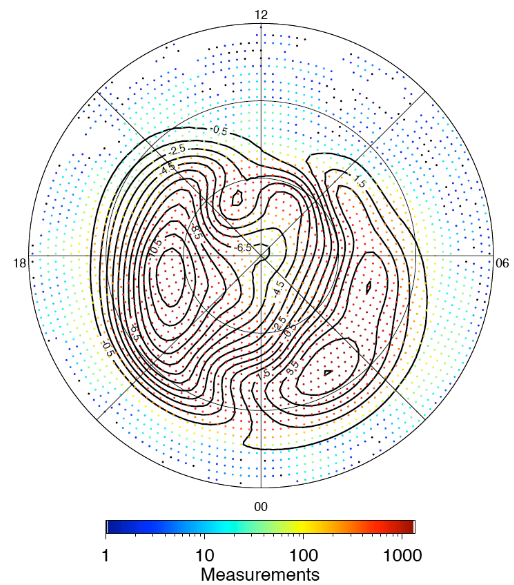

Figure A.1: Potential pattern for the bin with E_{RC} stability criteria within 2 to 4 kV/RE

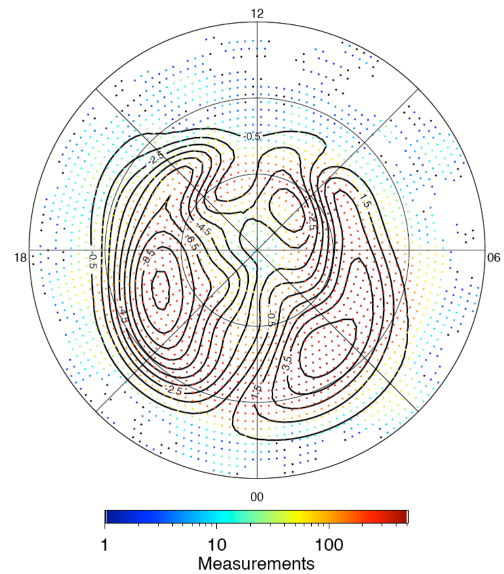

Figure A.2: Potential pattern for the bin with E_{RC} stability criteria within 4 to 6 kV/RE

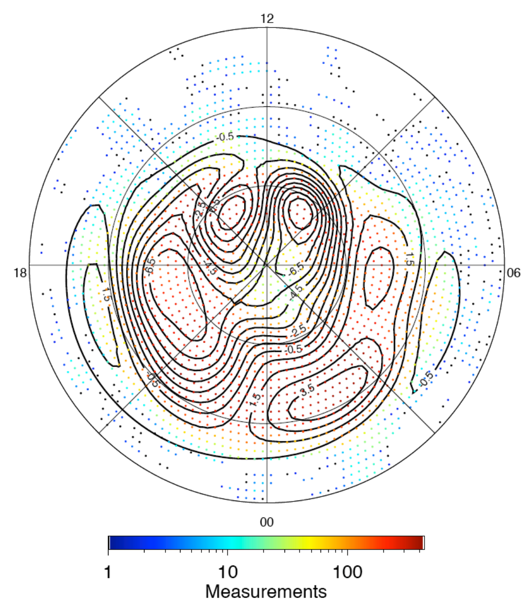

Figure A.3: Potential pattern for the bin with E_{RC} stability criteria within 10 to 13 kV/RE

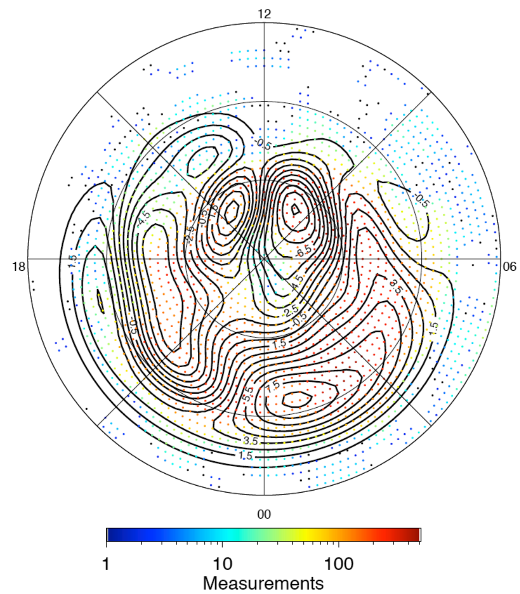

Figure A.4: Potential pattern for the bin with E_{RC} stability criteria within 12 to 15 kV/RE

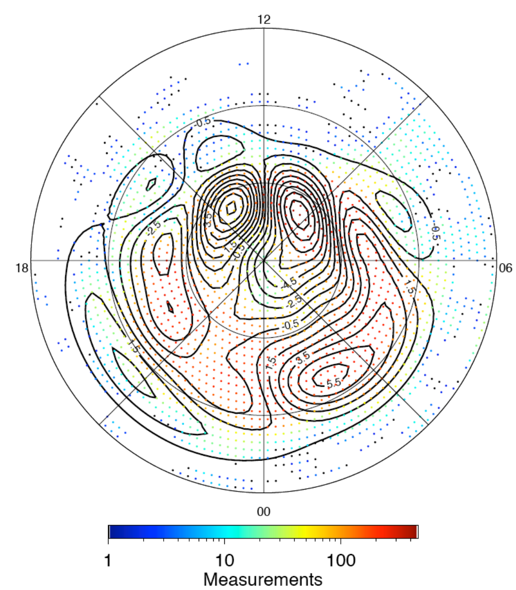

Figure A.5: Potential pattern for the bin with E_{RC} stability criteria within 13 to 16 kV/RE

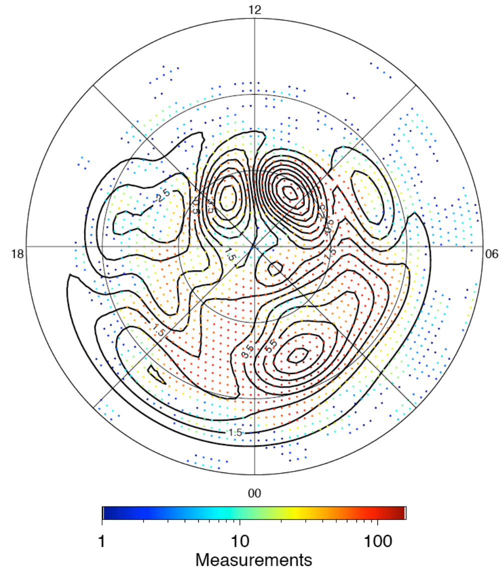

Figure A.6: Potential pattern for the bin with E_{RC} stability criteria within 14 to 18 kV/RE

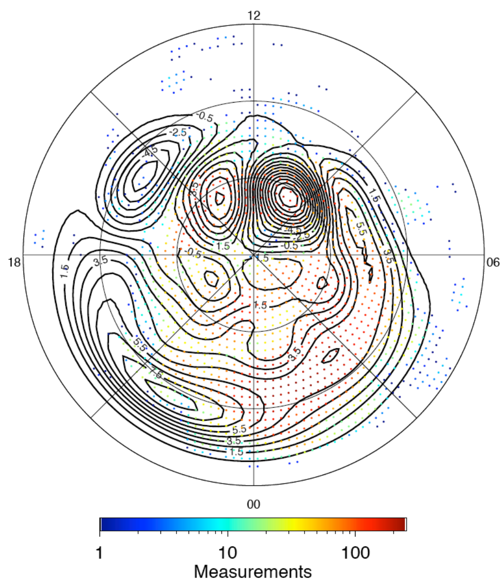

Figure A.7: Potential pattern for the bin with E_{RC} stability criteria within 16 to 19 kV/RE

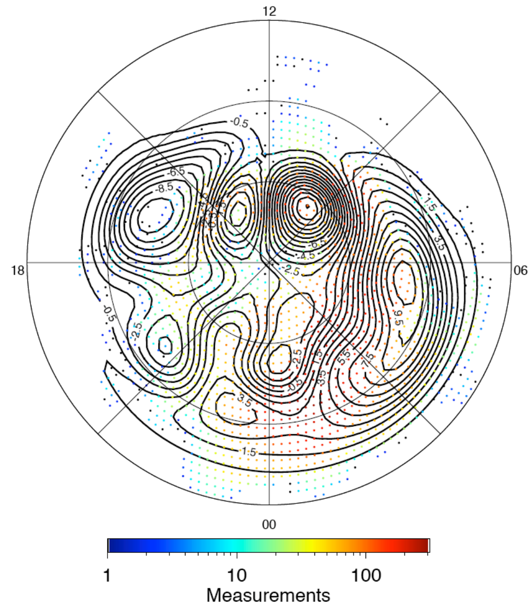

Figure A.8: Potential pattern for the bin with E_{RC} stability criteria within 16 to 21 kV/RE

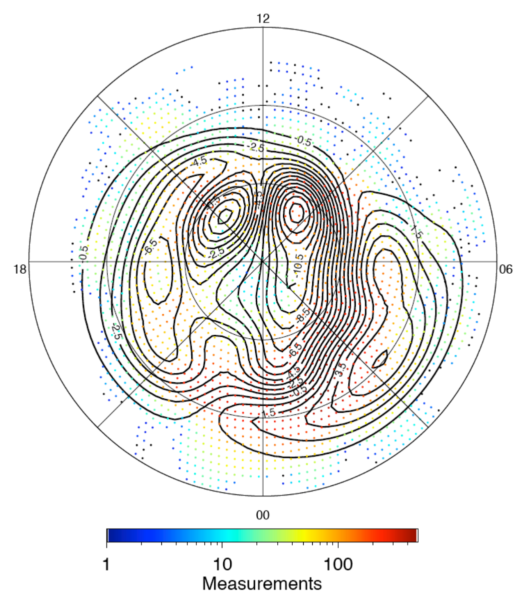

Figure A.9: Potential pattern for the bin with E_{RC} stability criteria within 18 to 22 kV/RE

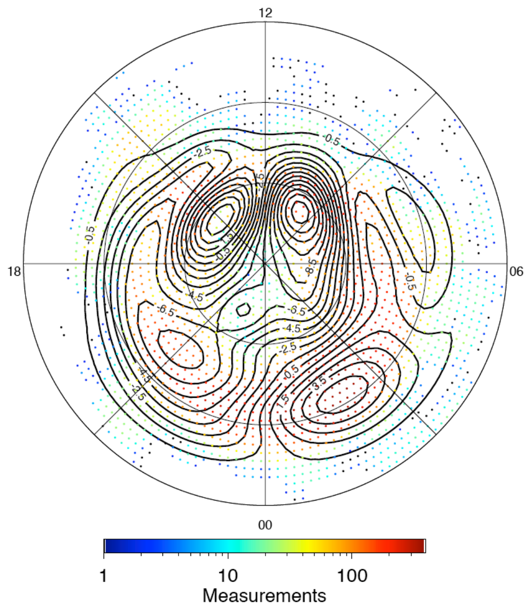

Figure A.10: Potential pattern for the bin with E_{RC} stability criteria within 19 to 23 kV/RE

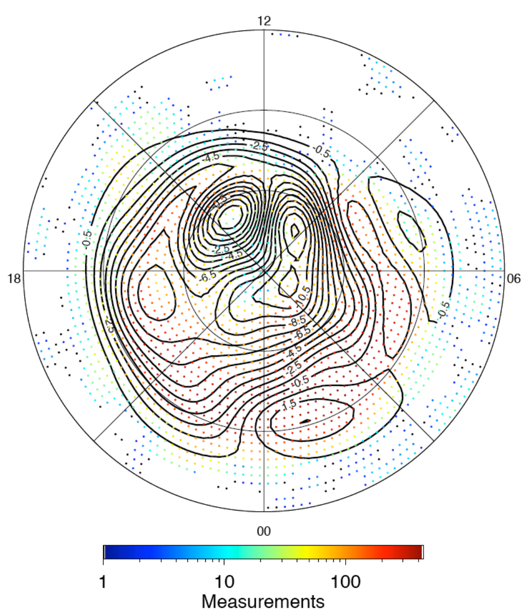

Figure A.11: Potential pattern for the bin with E_{RC} stability criteria within 20 to 24 kV/RE

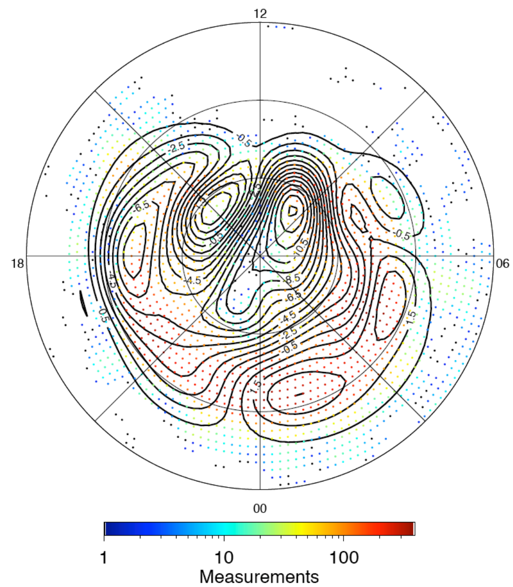

Figure A.12: Potential pattern for the bin with E_{RC} stability criteria within 21 to 25 kV/RE

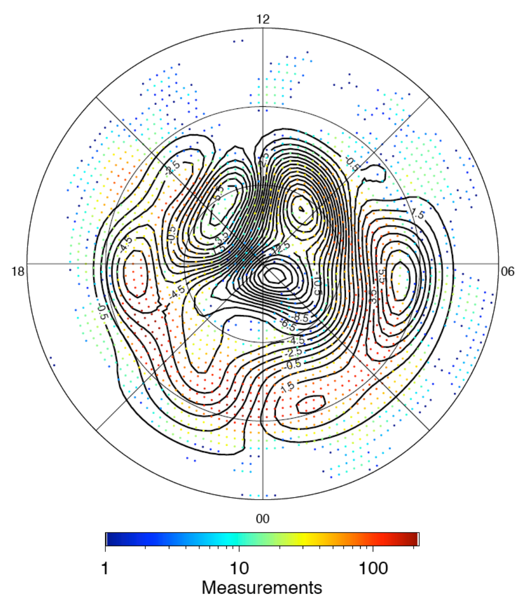

Figure A.13: Potential pattern for the bin with E_{RC} stability criteria within 22 to 26 kV/RE

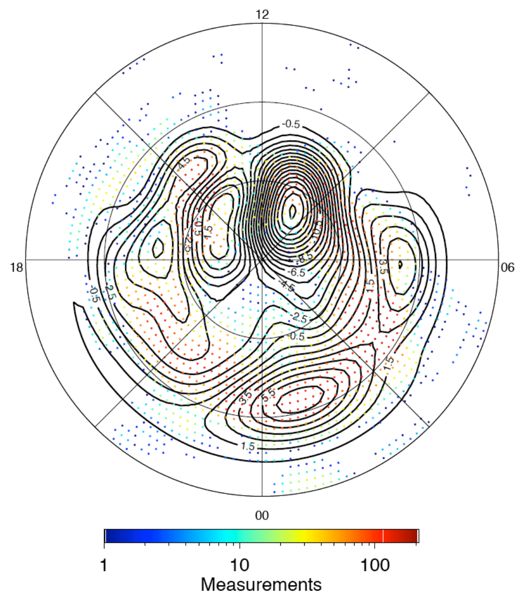

Figure A.14: Potential pattern for the bin with E_{RC} stability criteria within 23 to 27 kV/RE

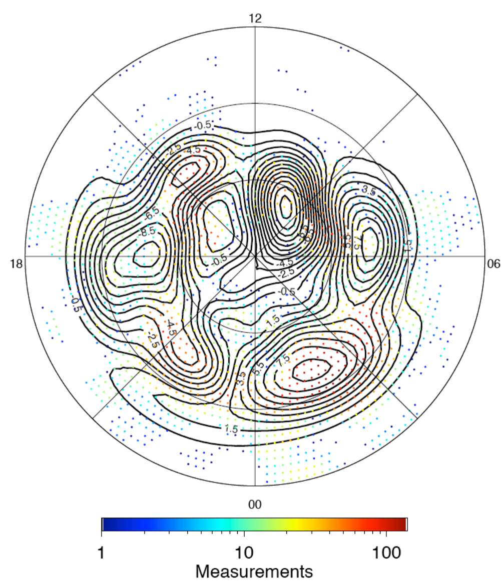

Figure A.15: Potential pattern for the bin with E_{RC} stability criteria within 24 to 28 kV/RE

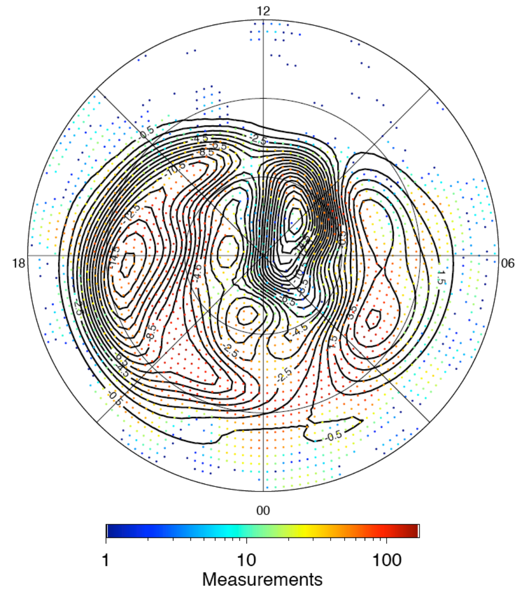

Figure A.16: Potential pattern for the bin with E_{RC} stability criteria within 25 to 30 kV/RE

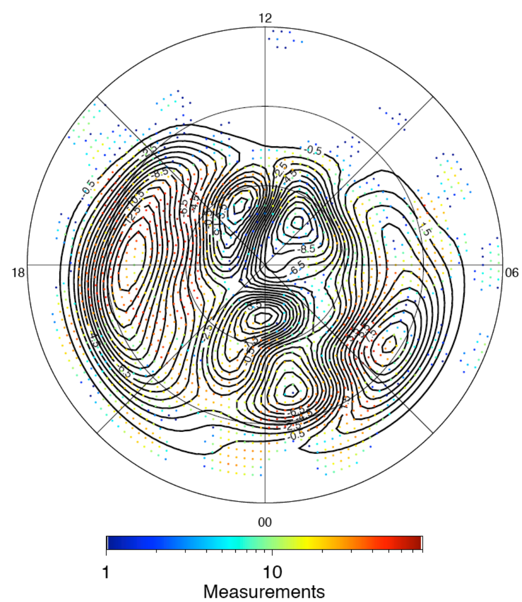

Figure A.17: Potential pattern for the bin with E_{RC} stability criteria within 27 to 32 kV/RE

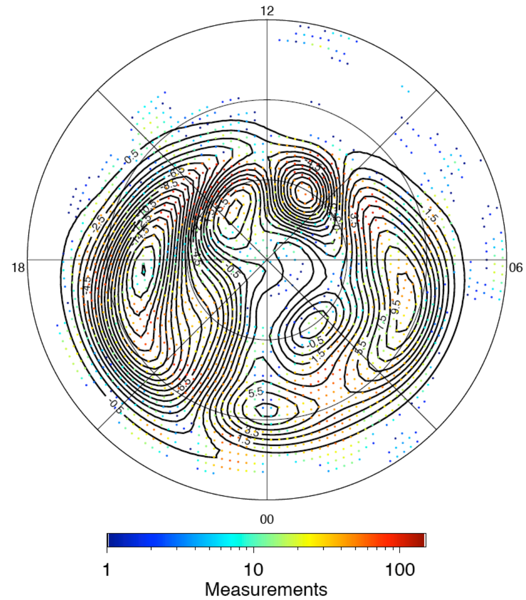

Figure A.18: Potential pattern for the bin with E_{RC} stability criteria within 28 to 36 kV/RE

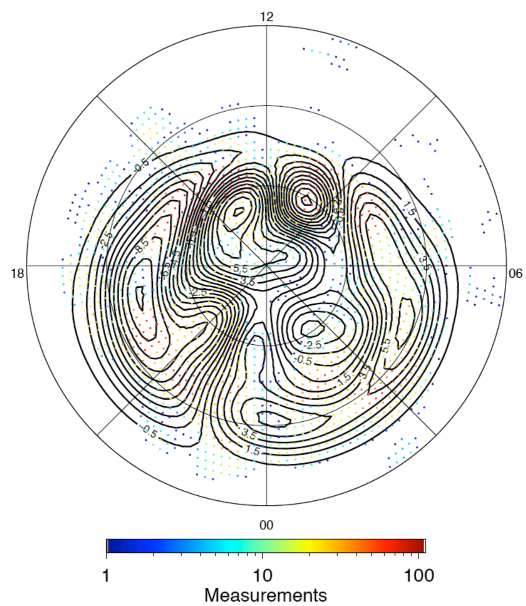

Figure A.19: Potential pattern for the bin with E_{RC} stability criteria within 30 to 36 kV/RE

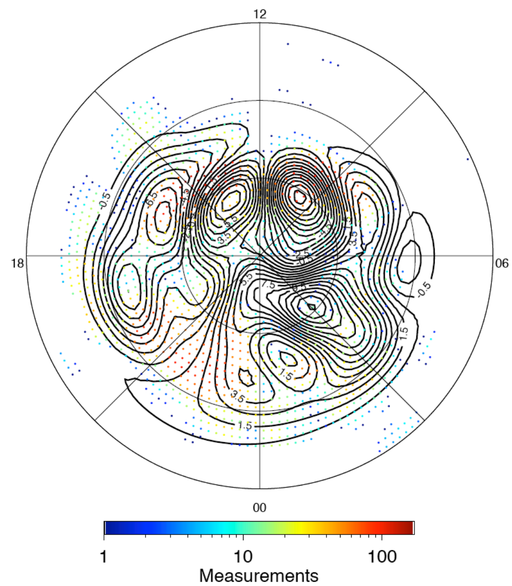

Figure A.20: Potential pattern for the bin with E_{RC} stability criteria within 31 to 38 kV/RE

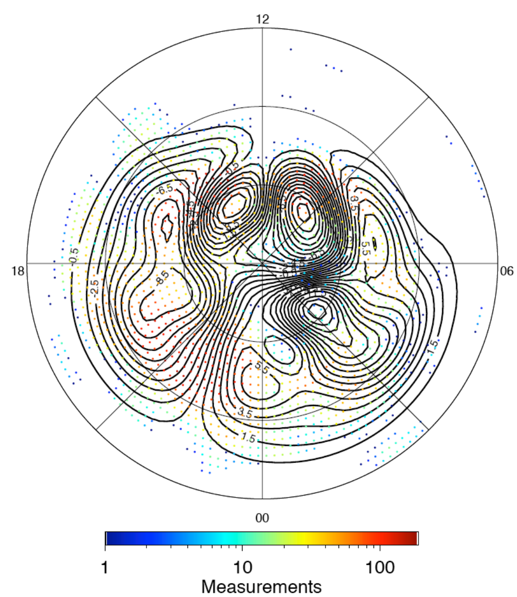

Figure A.21: Potential pattern for the bin with E_{RC} stability criteria within 31 to 40 kV/RE

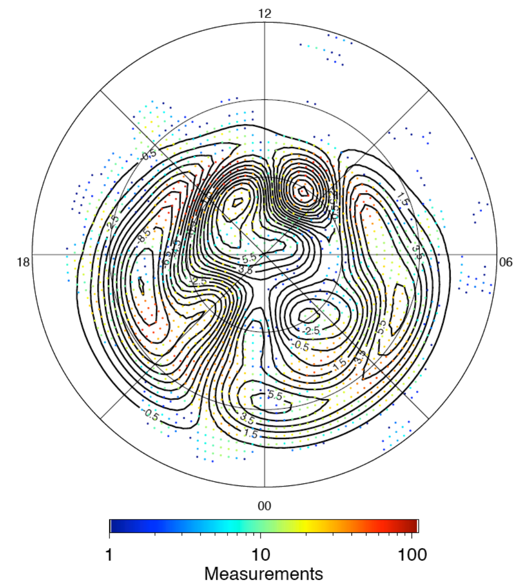

Figure A.22: Potential pattern for the bin with E_{RC} stability criteria within 32 to 36 kV/RE

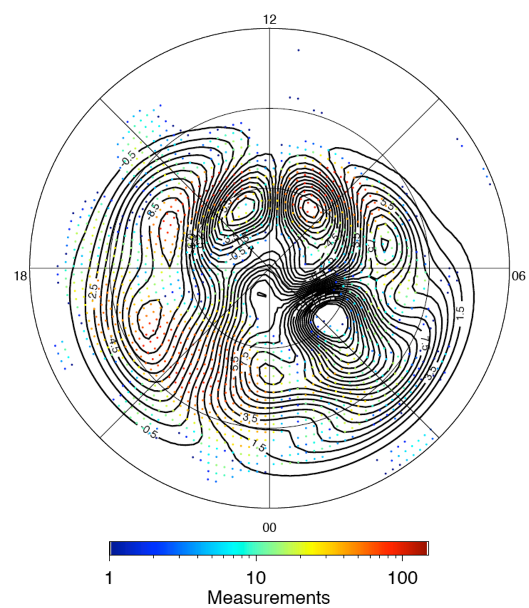

Figure A.23: Potential pattern for the bin with E_{RC} stability criteria within 32 to 39 kV/RE

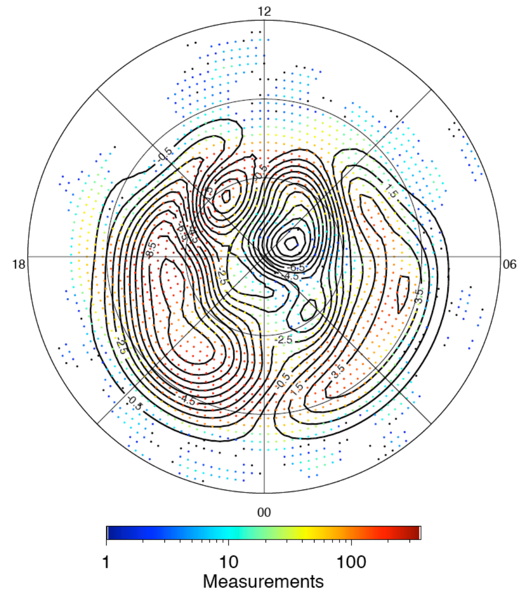

Figure A.24: Potential pattern for the bin with E_{RC} stability criteria within 37 to 47 kV/RE

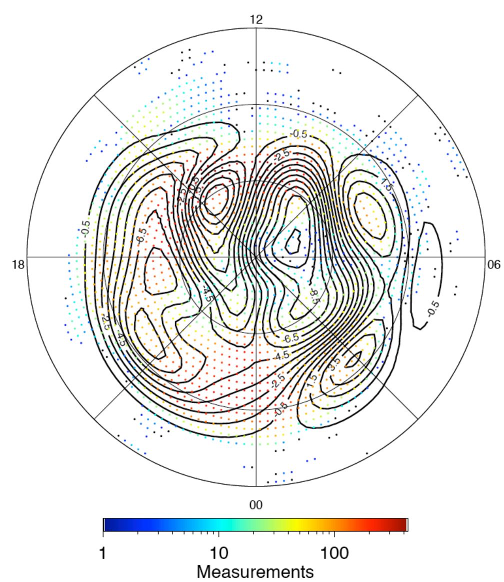

Figure A.25: Potential pattern for the bin with E_{RC} stability criteria within 40 to 50 kV/RE

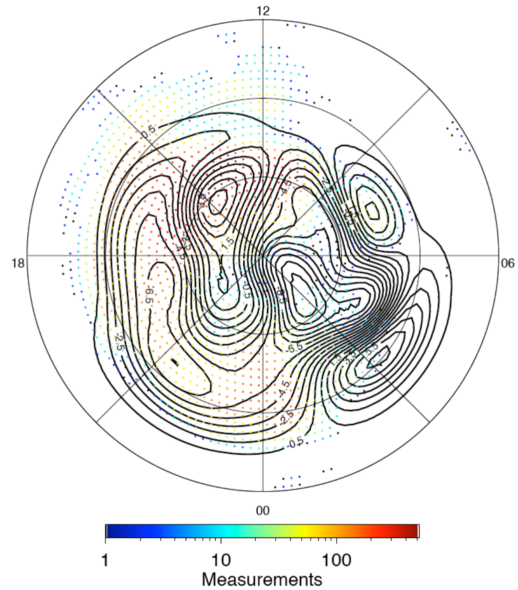

Figure A.26: Potential pattern for the bin with E_{RC} stability criteria within 43 to 53 kV/RE

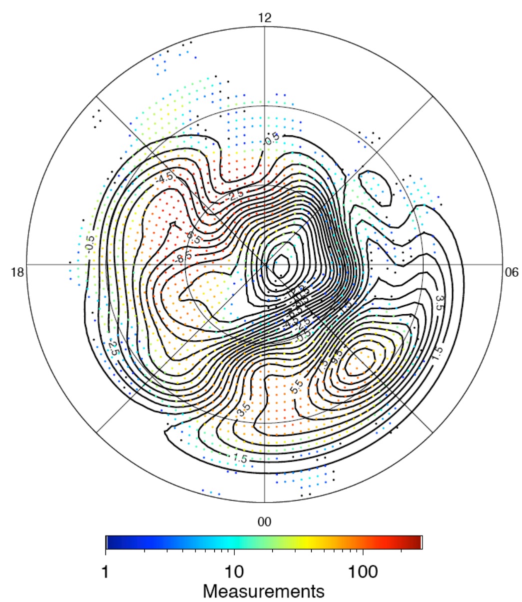

Figure A.27: Potential pattern for the bin with E_{RC} stability criteria within 46 to 56 kV/RE

BIBLIOGRAPHY

BIBLIOGRAPHY

Axford, W., and C. Hines, A unifying theory of high-latitude geophysical phenomena and geomagnetic storms, *Can. J. Phys.*, *39*, 1433, 1961.

Carlson, H., and A. Egeland, "The aurora and auroral ionosphere," in *Introduction to Space Physics,*edited by M.G. Kivelson and C.T. Russell*, p. 459*, Cambridge University Press, Cambridge, 1995.

Chen, F. F., *Introduction To Plasma Physics and Controlled Fusion Volume 1: Plasma Physics, Second Edition*, Springer, New York, 1974.

Chisham, G., et al., A decade of the super dual auroral radar network (superdarn): scientific achievements, new techniques and future directions, *Surveys in Geophysics*, *28*(1), 33–109, 2007.

Clauer, C. R., and E. Friis-Christensen, High latitude dayside electric fields and currents during strong northward imf: Observations and model simulation, *J. Geophys. Res.*, *93*, 2749, 1988.

Crooker, N. U., Reverse convection, *J. Geophys. Res.*, *97*, 19363, 1992.

Dorelli, J., A. Bhattacharjee, and J. Raeder, Separator reconnection at earth's dayside magnetopause under northward interplanetary magnetic field conditions, *J. Geophys. Res.*, *112*(A02202), doi:10.1029/2006JA011877, 2007.

Dungey, J. W., Interplanetary magnetic field and the auroral zones, *Phys. Rev. Lett.*, *6*, 47, 1961.

Friis-Christensen, E., and J. Wilhjelm, Polar cap currents for different directions of the interplanetary magnetic field in the $Y - Z$ plane, *J. Geophys. Res.*, *80*, 1248, 1975.

Gurnett, D., and A. Bhattacharjee, *Introduction to Plasma Physics With Space and Laboratory Applications*, Cambridge University Press, Cambridge, 2005.

Hairston, M., T. Hill, and R. Heelis, Observed saturation of the ionospheric polar cap during the 31 march 2001 storm, *Geophys. Res. Lett.*, *30*(6), doi:10.1029/2002GL015894, 2003.

Hill, T., A. J. Dessler, and R. A. Wolf, Mercury and Mars: The role of ionospheric conductivity in the acceleration of magnetospheric particles, *Geophys. Res. Lett.*, *3*, 429 – 432, 1976.

Hughes, W., "The magnetopause, magnetotail and magnetic reconnection," in *Introduction to Space Physics,*edited by M.G. Kivelson and C.T. Russell*, p. 227*, Cambridge University Press, Cambridge, 1995.

Hundhausen, A., "The solar wind," in *Introduction to Space Physics,*edited by M.G. Kivelson and C.T. Russell*, p. 91*, Cambridge University Press, Cambridge, 1995.

Iijima, T., T. A. Potemra, L. J. Zanetti, and P. F. Bythrow, Large-scale Birkeland currents in the dayside polar region during strongly northward IMF: A new Birkeland current system, *J. Geophys. Res.*, *89*, 7441, 1984.

Jackson, J. D., *Classical Eelectrodynamics*, John Wiley and Sons, New York, 1975.

Kan, J. R., and L. C. Lee, Energy coupling function and solar wind magnetosphere dynamo, *Geophys. Res. Lett.*, *6*, 577, 1979.

Karemcheti, K., *Principles of Ideal Fluid Aerodynamics*, Krieger, Malabar, 1966.

Kivelson, M., "Pulsations and magnetohydrodynamic waves," in *Introduction to Space Physics,*edited by M.G. Kivelson and C.T. Russell*, p. 330*, Cambridge University Press, Cambridge, 1995.

Kivelson, M. G., and C. T. Russell, Geophysical coordinate transformations, in *Introduction to Space Physics*, edited by M. G. Kivelson, and C. T. Russell, pp. 531–543, Cambridge University Press, Cambridge, UK, 1995.

Luhmann, J., "Ionospheres," in *Introduction to Space Physics,*edited by M.G. Kivelson and C.T. Russell*, p. 183*, Cambridge University Press, Cambridge, 1995.

Nagatsuma, T., Conductivity dependance of cross-polar potential saturation, *J. Geophys. Res.*, *109*, 2004.

Rees, M., *Physics and Chemistry of the Upper Atmosphere*, Cambridge University Press, Cambridge, 1989.

Reiff, P. H., and J. G. Luhmann, Solar wind control of the polar cap voltage, in *Solar Wind - Magnetosphere Coupling,* edited by Y. Kamide and J.A. Slavin*, p. 507*, Terra Scientific Publishing, Tokyo, Japan, 1986.

Richmond, A., and J. Thayer, "Ionospheric electrodynamics: A Tutorial", in Magnetospheric Current Systems, AGU Geophys. Monogr. Ser., Vol. 118, *edited by S. Ohtani, R. Fujii, M. Hesse, and R. L. Lysak, p. 131*, AGU, Washington, D.C., 2000.

Ridley, A. J., Estimations of the uncertainty in timing the relationship between magnetospheric and solar wind processes, *J. Atmos. Sol. Terr. Phys.*, *62*, 757, 2000.

Ruohoniemi, J., and S. K. Baker, Large-scale imaging of high-latitude convection with super dual auroral radar network hf radar observations, *J. Geophys. Res.*, *103*(A9), 20797–20811, 1998.

Ruohoniemi, J. M., and R. A. Greenwald, Statistical patterns of the high-latitude convection obtained from Goose Bay HF radar observations, *J. Geophys. Res.*, *101*, 21,743, 1996.

Ruohoniemi, J. M., R. Greenwald, K. Baker, J. Villain, and M. McCready, Drift motions of small-scale irregularities in the high-latitude f region: an experimental comparison with plasma drift motions, *J. Geophys. Res.*, *92*(A5), 4553–4564, 1987.

Russel, C. T., J. Luhmann, and G. Lu, Nonlinear response of the polar ionosphere to large values of the interplanetary electric field, *J. Geophys. Res.*, *106*(A9), 21083–21094, 2001.

Russell, C. T., "A brief history of solar-terrestrial physics," in *Introduction to Space Physics,*edited by M.G. Kivelson and C.T. Russell*, p. 227*, Cambridge University Press, Cambridge, 1995.

Sckopke, N., G. Paschmann, G. Haerendel, B. U. O. Sonnerup, S. J. Bame, T. G. Forbes, J. E. W. Hones, and C. T. Russell, Structure of the low-latitude boundary layer, *J. Geophys. Res.*, *86*, 2099–2110, 1981.

Shepherd, S., R. Greenwald, and J. Ruohoniemi, Cross polar cap potentials measured with super dual auroral radar network during quasi-steadi solar wind and interplanetary magnetic field conditions, *J. Geophys. Res.*, *107*(A7), doi:10.1029/2001JA000152, 2002.

Siscoe, G., J. Raeder, and A. Ridley, Transpolar potential saturation models compared, *J. Geophys. Res.*, *109*(A09203), doi:10.1029/2003JA010318, 2004.

Siscoe, G. L., N. U. Crooker, and K. D. Siebert, Transpolar potential saturation: Roles of region 1 current system and solar wind ram pressure, *J. Geophys. Res.*, *107*(A10), 2002a.

Siscoe, G. L., G. M. Erickson, B. U. O. Sonnerup, N. C. Maynard, J. A. Schoendorf, K. D. Siebert, D. R. Weimer, W. W. White, and G. R. Wilson, Hill model of transpolar potential saturation: Comparisons with MHD simulations, *J. Geophys. Res.*, *107*(A6), 2002b.

Song, Y., and R. Lysak, "Paradigm Transition in Cosmic Plasma Physics, Magnetic Reconnection and the Generation of Field-Aligned Current," in *Magnetospheric Current Systems, AGU Geophysical Monograph 118,*edited by S. Ohtani,

R. Fujii, M. Hesse and R.L. Lysak*, p. 11*, Cambridge University Press, Cambridge, 1995.

Stone, E., A. Frandsen, R. Mewaldt, E. Christian, D. Margolies, J. Ormes, and F. Snow, The advanced composition explorer, *Space Science Reviews*, *86*, 1–22, 1998.

Walker, R., and C. Russell, "Solar-wind interactions with magnetized planets," in *Introduction to Space Physics,*edited by M.G. Kivelson and C.T. Russell*, p. 164*, Cambridge University Press, Cambridge, 1995.

Weimer, D., Models of high-latitude electric potentials derived with a least error fit of spherical harmonic coefficients, *J. Geophys. Res.*, *100*, 19,595, 1995.

Weimer, D., Maps of field-aligned currents as a function of the interplanetary magnetic field derived from Dynamic Explorer 2 data, *J. Geophys. Res.*, *106*, 12,889, 2001.

Weimer, D., D. Ober, N. Maynard, M. Collier, D. McComas, N. Ness, C. Smith, and J. Watermann, Predicting interplanetary magnetic field (imf) propagation delay times using the minimum variance technique, *J. Geophys. Res.*, *108*(A1), doi:10.1029/2002JA009405, 2003.

Wolf, R., "Magnetospheric Configuration," in *Introduction to Space Physics,*edited by M.G. Kivelson and C.T. Russell*, p. 288*, Cambridge University Press, Cambridge, 1995.